

DRAFT VERSION JUNE 1, 2020

Typeset using L^AT_EX preprint style in AASTeX62

Cosmic spin and mass evolution of black holes and its impact

DIPANWEETA BHATTACHARYYA¹ AND A. MANGALAM¹¹*Indian Institute of Astrophysics, Sarjapur road, Koramangala 2nd Block, Bangalore-560034, India*

(Received 2019 September 5; Revised 2020 March 17; Accepted 2020 April 8)

Submitted to ApJ

ABSTRACT

We build an evolution model of the central black hole that depends on the processes of gas accretion, the capture of stars, mergers, and electromagnetic torque. In the case of gas accretion in the presence of cooling sources, the flow is momentum driven, after which the black hole reaches a saturated mass; subsequently, it grows only by stellar capture and mergers. We model the evolution of the mass and spin with the initial seed mass and spin in Λ CDM cosmology. For stellar capture, we have assumed a power-law density profile for the stellar cusp in a framework of relativistic loss cone theory that includes the effects of black hole spin, Carter’s constant, loss cone angular momentum, and capture radius. Based on this, the predicted capture rates of 10^{-5} to 10^{-6} yr⁻¹ are closer to the observed range. We have considered the merger activity to be effective for $z \lesssim 4$, and we self-consistently include the Blandford–Znajek torque. We calculate these effects on the black hole growth individually and in combination, for deriving the evolution. Before saturation, accretion dominates the black hole growth ($\sim 95\%$ of the final mass), and subsequently stellar capture and mergers take over with roughly equal contributions. The simulations of the evolution of the M_{\bullet} – σ relation using these effects are consistent with available observations. We run our model backward in time and retrodict the parameters at formation. Our model will provide useful inputs for building demographics of the black holes and in formation scenarios involving stellar capture.

Keywords: Black hole physics (159); Accretion (14); Stellar dynamics (1596); Cosmological evolution (336); Galaxy nuclei (609)

1. INTRODUCTION

It is now widely accepted that all massive galaxies have supermassive black holes (SMBHs) at their centers (Kormendy & Richstone 1995). At distances close to the center of these galaxies, stellar

Corresponding author: A. Mangalam

mangalam@iiap.res.indipanweeta@iiap.res.in

or gas motions are nearly completely dominated by the gravitational potential of the SMBH; this region is described as the sphere of influence. Black holes grow their mass and spin by accretion of gas, by the capture of stars, and by the merger activity of galaxies [that include the central black holes; Kesden et al. (2010)]. Here we discuss these processes to motivate our model of spin and mass evolution and its impact on various diagnostics like stellar capture rate, the M_{\bullet} - σ evolution, and retrodicting the properties of the seed black hole.

Alexander & Bar-Or (2017) have studied the evolution of the mass of the black holes by star capture, as well as accretion with and without merger activity. Nonrelativistic loss cone theory is used for their analysis, but the spin evolution of the black hole has not been considered. The loss cone is a region in velocity space where a star is captured by the black hole if it is within this region. The rates of tidal disruption events (TDEs) for a single black hole in steady state have been derived by different authors. Syer & Ulmer (1999) found the rate of capture to be 10^{-6} to 10^{-4} yr $^{-1}$ gal $^{-1}$ for main-sequence stars in the galaxies following the Nuker profile. Magorrian & Tremaine (1999) find the rate to be 10^{-9} to 10^{-4} yr $^{-1}$ gal $^{-1}$ using a two-integral model for nonspherical galaxies (triaxial) assuming that all the stars have centrophobic loop orbits and the refilling of loss cone occurs by the two-body relaxation process. Rauch & Tremaine (1996) found an enhancement in the rate of tidal disruption due to resonant relaxation processes for stars bound to the black hole, but Rauch & Ingalls (1998) find that in the presence of relativistic precession of black hole masses $\geq 10^8 M_{\odot}$, this effect is quenched. By assuming a single mass star distribution and solving the steady-state Fokker–Planck equation for 51 galaxies following the Nuker profile, Wang & Merritt (2004), derived the rate of disruption to be 10^{-9} to 10^{-4} yr $^{-1}$ with a revised M_{\bullet} - σ relation. Brockamp et al. (2011), using Aarseth’s NBODY 6 code, found the rate to be 10^{-6} to 10^{-4} yr $^{-1}$ gal $^{-1}$ assuming the Sersic profile with $n = 4$ for initial stellar distribution around the black hole. Kesden (2012) derived the capture rate in the presence of the spin of the black hole to be $\sim 10^{-5}$ to 10^{-6} yr $^{-1}$. Mageshwaran & Mangalam (2015) derived the rate of 10^{-4} – 10^{-5} yr $^{-1}$ for $M_8 = 10^{-2}$ to 10^2 in a nonrelativistic steady-state loss cone regime. Komossa (2015), Donley et al. (2002) (ROSAT surveys), and Gezari et al. (2009) (in UV band) have provided observed values of TDEs for different wavelength bands to be about 10^{-5} yr $^{-1}$.

The connection of the SMBHs to their host galaxies is evidenced by the strong correlation between the mass of SMBH and velocity dispersion, σ , of the stars in the rest of the galaxy. This is somewhat surprising because the velocity dispersion is measured for the stars that are too far from the SMBH to be affected by its gravitational field. Its origin is still a topic of debate. This relation is important since the mass of SMBH, which is very difficult to measure directly, can be calculated with relatively better precision using the quantity σ (the velocity dispersion of stars far from the SMBH), which is easier to measure for nearby systems. The cosmological M_{\bullet} – σ relation is given by the equation

$$M_{\bullet}(z) = K_0(z)\sigma^{p(z)}; \quad M_7 = k_0(z)\sigma_{100}^{p(z)}, \quad (1)$$

where $M_7 = M_{\bullet}/10^7 M_{\odot}$ and $\sigma_{100} = \sigma/(100 \text{ km sec}^{-1})$. The value of $k_0(0)$ is typically $\simeq 1$ [see Table 7]. Ferrarese & Merritt (2000) first reported the index p of the relation to be 4.8 ± 0.5 , which can be explained, for example, by the gas feedback argument of Silk & Rees (1998) based on energy-driven flow. Gebhardt et al. (2000) reported p to be 3.75 ± 0.3 , which is close to the prediction of $p = 4$ given by a feedback argument by King (2003) based on momentum-driven flow. The exact explanation of the origin of this relation is still not understood properly, but various models give p between 4

and 5, which is in rough agreement with observations as summarized in [Bhattacharyya & Mangalam \(2018\)](#). [Shankar et al. \(2009a\)](#) renormalized Equation (1) using $k_0 \rightarrow k_0(1+z)^\alpha$ and found $\alpha = 0.33$. [Ferrarese \(2002\)](#) finds the M_\bullet - σ relation to be valid until $z \simeq 1$ (the limit of the survey) and expects that the relation was likely to hold beyond $z = 1$.

[Merritt & Ferrarese \(2001\)](#) have analyzed a sample of 32 galaxies to determine the ratio of bulge mass and black hole mass using the M_\bullet - σ relation. The mass density of the black hole in the local universe is consistent with the observations. The local black hole scaling relations (with σ and bulge mass, M_b), given by [Salucci et al. \(1999\)](#) were used to derive a black hole mass function ([Shankar 2013](#)). The redshift variation of the scaling relations has been taken to be $\propto (1+z)^\alpha$ and the value of α has been determined for M_\bullet - M_b , as well as the M_\bullet - σ relation, and thus the black hole mass density has been determined. [Netzer \(2010\)](#) has derived the evolution of M_\bullet and L/L_{Edd} with redshift for type 1 radio-quiet active galactic nuclei (AGNs).

The mass evolution equation for black holes (ignoring mergers) can be approximated by

$$M_\bullet(t) = f(t)\mathcal{M} = K_0\sigma^p \simeq M_s + \int dt(\dot{M}_* + \dot{M}_g) \simeq K_0(t)\sigma^{p(t)} \quad (2)$$

where $\dot{M}_* = \langle m_* \rangle \dot{N} = k_2\sigma^{p_1}$, where $p_1 = 4.3$ for nonrelativistic loss cone theory (eg. [Mageshwaran & Mangalam \(2015\)](#)), and $\dot{M}_g = k_1\sigma^{p_2}$ where $p_2 \simeq 4$ is the gas accretion rate from the momentum-driven flow. The seed black hole mass is derived from black hole formation models and is roughly given by $M_s \propto \mathcal{M}$ or $M_s = k_3\sigma^{p_3}$ (Faber–Jackson law by a fiducial argument here gives $p_3 \simeq 5$), although p_3 is quickly irrelevant as $M_\bullet \gg M_s$ during the evolution. The similarity of $p_1 \simeq p_2 \simeq p_3$ is why we think that the form of the M_\bullet - σ relation approximately holds at all epochs; hence, Equation (2) is the basic paradigm of the paper with a model to predict p , given an evolutionary model of mass and spin. While nonrelativistic simulations ([Shankar et al. 2009a](#); [Sijacki et al. 2015](#)) obtained the evolution of the M_\bullet - σ relation previously, we have derived here the *joint* evolution of the mass and spin of SMBH using a semianalytic model that takes into account the relativistic effects on the critical radii like the horizon, the capture radius, and the cross section that is incorporated into our steady loss cone formalism. Further, our calculations consider all the possible factors contributing to the growth of black holes like accretion, stellar capture, mergers, and Blandford–Znajek (BZ) torque simultaneously; previously, there were models for determination of the evolution for different factors separately. We have built a model for the evolution of measured spin of black holes and estimated its impact on the M_\bullet - σ relation in Λ CDM cosmology, which is predicated on the physics of gas accretion, star capture, and mergers. We have self-consistently solved coupled equations to get a more complete picture of the evolution of the spin and mass of the SMBH. Our results are shown to agree well with a preliminary analysis of observational data of different galaxies.

From the analysis of [Bardeen et al. \(1972\)](#), without thermodynamic effects, the nonrotating black holes can attain a maximum spin of ≈ 1 by the accretion of gas from the innermost stable circular orbit (ISCO). The black hole spin is limited by an upper limit of the spin of 0.998 based on radiation torque due to a difference in cross section for counter and corotating photons near this limit, which is responsible for the saturation ([Thorne 1974](#)). From Seyfert 1.2 galaxy MCG-06-20-15, XMM-Newton observations have analyzed the upper limit to be $0.989_{-0.002}^{+0.009}$ with 90% confidence ([Brenneman & Reynolds 2006](#)). Later on, [Gammie et al. \(2004\)](#) have found the maximum value to be around 0.9, less than 0.998 for relativistic MHD disks. This may not be applicable for thin disc cases; this suggests that the black holes that have grown through MHD accretion are not maximally rotating.

For the thick-disk cases, the saturated value of spin was found to be 0.93. The thin-disk analysis by [Gammie et al. \(2004\)](#) indicates that through sub-Eddington accretion, the spin can be very close to the maximal rotation. [Volonteri et al. \(2005\)](#) and [Volonteri & Rees \(2005\)](#) have argued that the effect of accretion torque always results in spinning up of the black hole. In the former paper, the spin-up process of black holes is assumed to be caused by the accretion and binary coalescence, where the SMBH spins up even if the direction of the spin axis varies with time as accretion dominates over coalescences. But if the accretion disks become self-gravitating, their angular momentum per unit mass will be less than that of the black hole. Therefore, in such cases, a black hole having sufficient spin will be spun down ([King et al. 2008](#)). If the black hole is growing by the merger process, the upper limits can be different. After extrapolation of data, [Marronetti et al. \(2008\)](#) have suggested that, for merging two similar-mass black holes with maximum initial spin and aligned with their orbital angular momentum, the upper value can be 0.951 ± 0.004 . [Volonteri & Rees \(2005\)](#) have calculated the growth of black holes taking the range of the formation redshift as $z_f \sim 10\text{--}20$, using an accretion rate given by the Bondi–Hoyle formula which is $\propto M_\bullet^2$.

Our goal in this paper is to consider all these processes: gas accretion, stellar capture, mergers, and black hole electro-dynamical spin-down to build a self-consistent model of spin and mass evolution. The main motivation of this study is to construct a detailed evolution model of the black hole, that can be a useful tool to study the coevolution of the black hole and the galaxy. We take a comprehensive approach by including all the growth channels semianalytically, with an aim to isolate the important effects. The relativistic treatment is important, as all the channels depend on spin and hence would modulate the black hole growth. The mass evolution equation taking into account gas accretion, stellar capture, and mergers is given by

$$\frac{dM_\bullet}{dt} = \epsilon_I(j)\dot{M}_{\bullet g} + \epsilon(j)\dot{M}_{\bullet*} + \dot{M}_{\bullet m}, \quad (3)$$

and the evolution equation for the spin parameter, j , is given by

$$\frac{dj}{dt} = \frac{\dot{M}_{\bullet g}}{M_\bullet} \left(l_I(j) - 2\epsilon_I(j)j \right) + \frac{\dot{M}_{\bullet*}}{M_\bullet} \left(l_*(j) - 2\epsilon(j)j \right) + \dot{M}_{\bullet m} \cdot \frac{j}{M_\bullet} \left(-\frac{7}{3} + \frac{9q}{\sqrt{2}j^2} \right) + x_+^3(j)j \frac{\mathcal{G}_0}{\mathcal{J}_0}, \quad (4)$$

where the first three terms in Equations (3) and (4) are for accretion, stellar capture, and mergers, respectively, while the last term in Equation (4) arises as a result of the BZ torque. The mass accretion efficiency, $\epsilon(j)$, is given by

$$\epsilon(j) = \begin{cases} \epsilon_I(j) & \text{for } M_\bullet < M_c \\ 1 & \text{for } M_\bullet \geq M_c, \end{cases} \quad (5)$$

where M_c is the critical mass defined in Section 2.2, and

$$\epsilon_I(j) = \frac{z_m^2(j) - 2z_m(j) + j\sqrt{z_m(j)}}{z_m(j)(z_m^2(j) - 3z_m(j) + 2j\sqrt{z_m(j)})^{1/2}}, \quad (6)$$

is the efficiency of gas accretion through ISCO, where the ISCO radius is given by ([Bardeen et al. 1972](#))

$$z_m(j) = \frac{r_{ms}}{M_\bullet} = 3 + Z_2 - k\sqrt{(3 - Z_1)(3 + Z_1 + 2Z_2)}; \\ Z_1 = 1 + (1 - j^2)^{1/3}((1 + j)^{1/3} + (1 - j)^{1/3}); Z_2 = (3j^2 + Z_1^2)^{1/2}, \quad (7)$$

where $k = 0$ for $j = 0$, $+1$ for prograde and -1 for retrograde cases, and $j \in \{0, 1\}$. We will derive and discuss each term in Equations (3) and (4) in the next section. The symbols used in these equations are defined in Table 1. Figure 7 and Table 2 in Section 2 show the domains of operation and the strengths of the terms (calculated in Appendix D), respectively. The solution of these two equations will provide the joint mass and spin evolution of black holes. This self-consistent evolution model would be handy in comparing results with simulations and in retrodictions of the formation parameters, thus constraining models of black hole formation. In the future, detailed demographic studies can be carried out to evolve black hole mass and spin distributions. The three applications that we consider are as follows: The first is the capture rates of stars taking into account relativistic corrections to the tidal radius and the capture radius (Rana & Mangalam 2019a) to the loss cone model given by Mageshwaran & Mangalam (2015). Second, using the model, we predict the evolution of the $M_{\bullet}-\sigma$ relation. The third application is to retrodict the seed mass and spin of the black hole and the formation redshift under various assumptions, given the recent observations at the epoch near $z \simeq 7$ (Campitiello et al. 2019).

In Table 1, a glossary of the symbols used is given. In Section 2 we discuss the growth of the SMBH by gas accretion, star capture, mergers, and the effects of BZ torque on the spin evolution of the black hole individually and discuss the individual evolution equations. In Section 3, we build the required collective evolution equations for spin and mass of SMBH and discuss the cumulative effects. In Section 4, we discuss the impact on the $M_{\bullet}-\sigma$ relation, and we also retrodict from the known parameters of mass and spin of the quasars ULASJ134208.10+092838.61 ($z = 7.54$), ULASJ112001.48+064124.3 ($z = 7.08$) and DELSJ003836.10-152723.6 ($z = 7.02$) (Campitiello et al. 2019), the seed spin, and the mass of the black holes. In Section 4.3 we summarize the results. The discussions are presented in Section 5 and the conclusions in Section 6.

Common Parameters			
M_\bullet	Mass of the black hole	j	Spin parameter of the black hole
M_s	Seed black hole mass	t_0	Unit of time (1 Gyr)
j_0	Seed black hole spin parameter	p	Index of the M_\bullet - σ relation
M_b	Bulge mass	σ	Velocity dispersion of stars
f_b	M_\bullet/M_b	M_\odot	Solar mass
M_x	$M_\bullet / 10^2 M_\odot$	σ_x	$\sigma/(x \text{ km sec}^{-1})$
G, c	Gravitational constant, speed of light	r_g	GM_\bullet/c^2
t, z	Look-back time and redshift	z_f	Formation redshift
Ω_m, a	Cosmological parameter, scale factor	H_0	Hubble constant
μ_\bullet	M_\bullet/M_s	t_0	1 Gyr
Gas dynamical parameters			
$\dot{M}_{\bullet g}$	Rate of mass growth by accretion	η	Efficiency factor of Eddington accretion = $\dot{M}_\bullet/\dot{M}_E$
ϵ_M	Radiation efficiency= $L/\dot{M}_0 c^2$, where L is luminosity, \dot{M}_0 is rest mass accretion rate		
Stellar dynamical parameters			
x_c, x_ℓ	Capture and loss cone radius in units of r_g	l_ℓ	Angular momentum in units of $\frac{GM}{c}$ at x_ℓ
l_p, l_{tr}	Angular momentum in units of $\frac{GM}{c}$ at x_c	x_t	Tidal radius in units of r_g
η_t	Strength of tidal encounter	r_p	Radius of pericenter
x_+	Horizon in units of r_g	V_{eff}	Effective potential in Kerr metric
m_*	Mass of a star	R_*	Radius of a star
l_ℓ	Loss cone angular momentum	ρ	Stellar mass density
γ	Power-law index of mass density	P	Radial orbital period
$f_s(E)$	Distribution function of stars	\dot{N}_f, \dot{N}_s	Rate of capture of stars in full and steady loss cone
q_s	Diffusion parameter	J	Orbital angular momentum
J_c	Angular momentum of circular orbit	E	Orbital energy
r_h	Influence radius of black hole	s_t	r_t/r_h
ϵ	E/σ^2 , normalized energy	$\dot{M}_{\bullet*}$	Rate of mass growth by stellar capture
Mergers and BZ torque			
q	Merger mass ratio	$\dot{M}_{\bullet m}$	Rate of growth of mass by mergers
\dot{N}_m	Rate of mergers	\mathcal{J}_0	Angular momentum budget of black hole
\mathcal{G}_0	BZ torque	B_4	Magnetic field in units of 10^4 G
f_h	Ratio of black hole mass to the halo mass		
Evolution			
$M_{\bullet t}$	Saturation mass	t_s	Saturation time
z_s	Saturation redshift	μ_M	Ratio of mass gained and seed mass
$M_{\bullet c}$	Critical mass below which $\dot{M}_{\bullet*} > \dot{M}_{\bullet g}$		

Table 1. Glossary of Symbols Used.

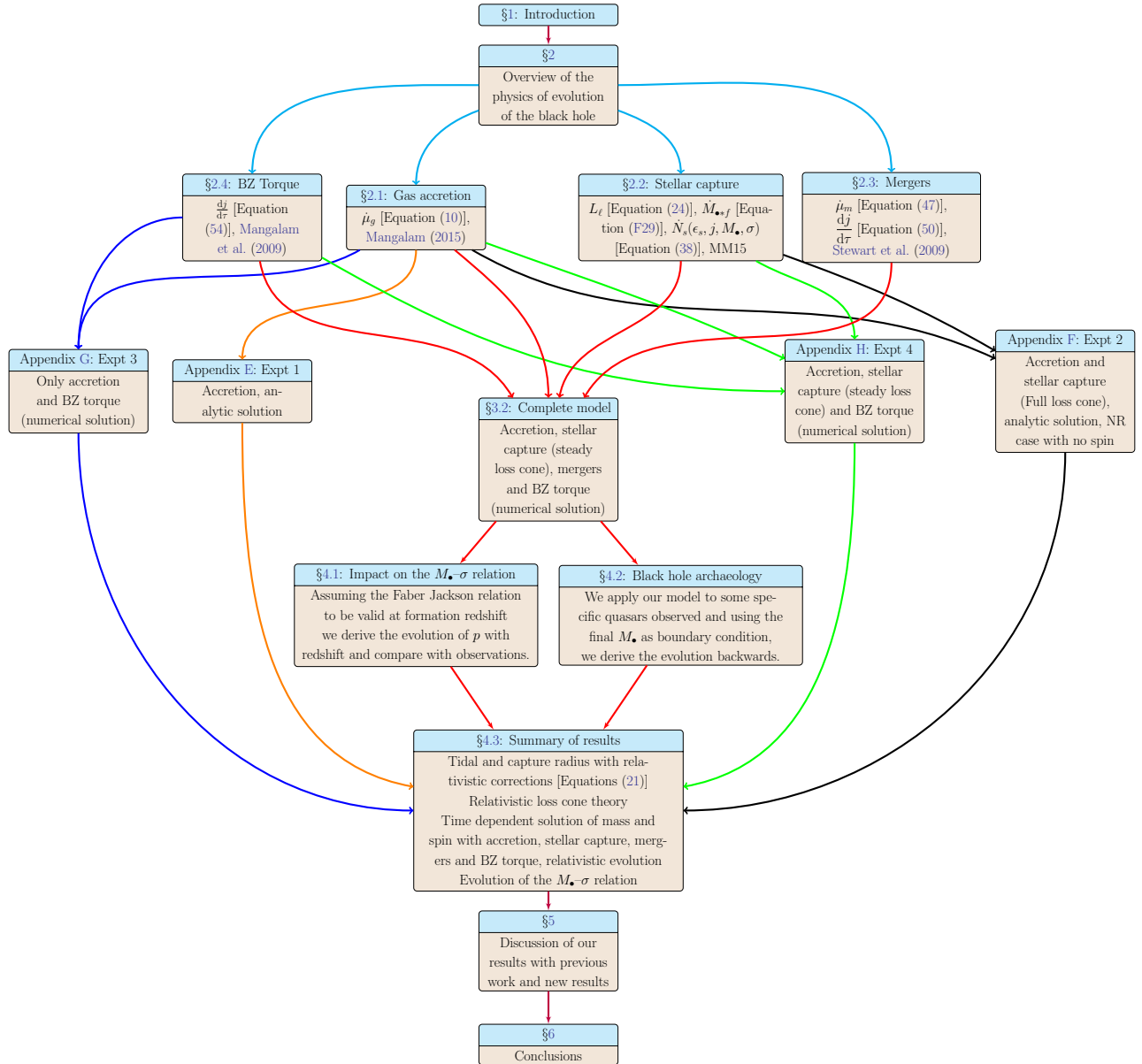


Figure 1. Flowchart of concepts in the paper discussing the input physics of relativistic stellar capture, gas accretion, electromagnetic torque and mergers

2. OVERVIEW OF THE PHYSICS OF EVOLUTION OF THE BLACK HOLE

The seed black holes grow their mass mainly through three processes: accretion, stellar capture, and mergers. Though the stellar capture presumably does not contribute to the evolution of its spin, the other two do contribute to spin evolution. The BZ mechanism (Blandford & Znajek 1977) of electromagnetic braking of the black hole contributes to spinning, but it does not have any effect on mass growth. In this section, we discuss all these processes individually, derive Equations (3) and (4) and state the assumptions of our model.

2.1. *Growth of the Black Hole by Gas Accretion*

The black hole mainly grows by accretion flow of the gas. In the case of an energy-driven flow (Silk & Rees 1998) it is assumed that all the energy from the accretion is used for unbinding the mass of the bulge and the maximum possible mass the SMBH can attain from this accretion process is

$$M_{\bullet} \simeq 8 \times 10^8 \left(\frac{\sigma}{300 \text{ km sec}^{-1}} \right)^5 M_{\odot}. \quad (8)$$

King (2003) proposed that black hole growth occurs by gas flow until it reaches a saturated mass $M_{\bullet,t}$, which is a different approach than that of Silk & Rees (1998), who propose an energy-driven flow by assuming that the energy from accretion is completely used in unbinding the mass of the galactic bulge, while there is no loss of energy due to radiation. King (2003) considers Compton cooling, for which some energy is lost to radiation and the remaining energy is available for unbinding the mass of the bulge. From the analysis of King (2003) after saturation, the outflow velocity exceeds the escape velocity of the medium and the gas is driven away, causing the accretion process to stop. The saturated mass is found to be $M_{\bullet,t} = 9.375 \times 10^6 \sigma_{100}^4 M_{\odot}$ derived for a spherical geometry of the ambient gas. However, the infalling matter must possess some amount of angular momentum so that an accretion disk forms, and thus there is a small solid angle where only inflow occurs. If most of the gas lies in the plane of the galaxy, the momentum-driven outflow would not halt the inflow; this also implies that accretion from this point adds little mass to the hole. In our model, we ignore accretion after saturation and consider that only stellar capture and mergers contribute to the growth of the black hole and also at this point $p \approx 4$. We take sub-Eddington accretion throughout so that

$$\dot{M}_{\bullet,g} = k_1 M_{\bullet}, \quad (9)$$

where $k_1 = \frac{4\pi G m_p \eta}{\sigma_e c}$ and the factor $\eta = \dot{M}_{\bullet} / \dot{M}_E$, where \dot{M}_E is the Eddington accretion rate.

Therefore, in units of $\mu_{\bullet} = \frac{M_{\bullet}}{M_s}$, where M_s is the seed mass, $\tau = \frac{t}{t_0}$, where $t_0 = 1$ Gyr, we can express

$$\dot{\mu}_g = \frac{\dot{M}_{\bullet,g} t_0}{M_s}. \quad (10)$$

Mangalam (2015) used a theoretical model for mass and spin evolution of the black hole taking into account the angular momentum torque caused by the electro-dynamical jet, where it was shown that the spin evolution with the accretion rate is taken to be a given fraction of the Eddington rate for different cases such as the thin disk, Bondi accretion, and also MHD disk. The mass evolution equation is given by

$$\frac{dM_{\bullet}}{dt} = \epsilon_I(j) \dot{M}_{\bullet,g}, \quad (11)$$

where $\epsilon_I(j)$ [see Equation (2)] is the efficiency of energy conversion with the innermost radius of the disk to be taken typically at ISCO, and $\dot{M}_{\bullet,g}$ is the rate of accretion. The spin evolution equation is given by [see Mangalam (2015), Mangalam et al. (2009), Shapiro (2005)]

$$\frac{dj}{dt} = \frac{\dot{M}_{\bullet,g}}{M_{\bullet}} \left(l_I(j) - 2\epsilon_I(j)j \right), \quad (12)$$

where $l_I(j)$ [see Equation (5)] is the angular momentum per unit mass at ISCO. This can be seen by the following arguments. The first term is due to the accretion of angular momentum at ISCO, while the second represents the spin-down due to an increase in the black hole inertia; these arguments give

$$J_{\bullet} = \frac{GM_{\bullet}^2 j}{c},$$

$$\dot{j} = \frac{c}{G} \frac{d}{dt} \left[\frac{J_{\bullet}}{M_{\bullet}^2} \right] = \frac{\dot{M}_{\bullet} g}{M_{\bullet}} \left(l_I(j) - 2\epsilon_I(j)j \right). \quad (13)$$

2.2. Growth of the Black Hole by stellar capture

The SMBHs can also grow by the capture of stars in two ways. Those stars that fall into the event horizon without disruption are directly captured, and the indirect capture occurs when the stars are tidally disrupted outside the horizon. For SMBHs more massive than $10^8 M_{\odot}$, the direct capture of solar-type stars is possible if the angular momentum of the star is smaller than some critical value (Frank & Rees 1976) for the nonrelativistic case. We proceed to calculate the limiting value for the relativistic case. For a Kerr black hole, the standard effective potential is written as [Carter (1968); Misner et al. (1973); Frolov & Novikov (1998); Rana & Mangalam (2019a); Rana & Mangalam (2019b) (RM19)]

$$V_{eff}(x, l, j, Q) = -\frac{1}{x} + \frac{l^2 + Q}{2x^2} - \frac{[(l-j)^2 + Q]}{x^3} + \frac{j^2 Q}{2x^4}. \quad (14)$$

Here $l \equiv L/(GM/c)$, where L is the angular momentum, $x = r/r_g$, $r_g = GM_{\bullet}/c^2$, j is the spin parameter, and Q is the Carter's constant. The solution of $V_{eff}(x_p) = 0$ and $V'_{eff}(x_p) = 0$ gives the equation of separatrix orbit where x_p is the pericenter, as shown in Fig 2(b) of RM19. From the two conditions $V_{eff}(x_p) = 0$ and $V'_{eff}(x_p) = 0$, we find the equation for the separatrix $x_p(Q, l, j)$ to be given by

$$x_p^3 - [(l-j)^2 + Q]x_p + j^2 Q = 0, \quad (15)$$

which represents a turning point condition for an orbit that is just bound or just unbound. This also represents a marginally bound spherical orbit (MBSO). The innermost stable spherical orbit (ISSO) and MBSO are the end points of the separatrix curve from ($e = 0$, ISSO) to ($e = 1$, MBSO). The star is captured at MBSO (as $r \rightarrow \infty$ in Figure 2(b) of RM19) and r_s is the pericenter. This capture radius (MBSO) $x_c(Q, j)$ in units of r_g , is found by reducing Equation (15) to (by substituting for $(l-j)$ from the translation formulae [see Equation (7) in RM19]; see Appendix D of RM19 for details)

$$\begin{aligned} x_c^8 - 8x_c^7 - 2j^2 x_c^6 + 16x_c^6 + 2j^2 Q x_c^5 - 8j^2 x_c^5 - 6j^2 Q x_c^4 + j^4 x_c^4 - 2j^4 Q x_c^3 + \\ 8j^2 Q x_c^3 + j^4 Q^2 x_c^2 - 2j^4 Q x_c^2 - 2j^4 Q^2 x_c + j^4 Q^2 = 0. \end{aligned} \quad (16)$$

Solving Equation (16) for real roots (numerically for $Q \neq 0$) that are higher than the light radius (Bardeen 1973), we find the capture radii for both prograde and retrograde cases. If $Q = 0$, Equation (16) reduces to

$$x_c^4(x_c^2 - 2jx_c + j^2 - 4x_c)(x_c^2 - 4x_c + j^2 + 2jx_c) = 0, \quad (17)$$

which leads to the known result (Zhao et al. 2002)

$$x_c(j) = \begin{cases} -j + 2(1 + \sqrt{1-j}) & \text{for prograde} \\ j + 2(1 + \sqrt{1+j}) & \text{for retrograde} \end{cases} \quad (18)$$

The angular momentum at x_c , from Equation (15), is found to be

$$l_c(M_8, j, Q) = j + k \sqrt{x_c^2 - Q + \frac{j^2 Q}{x_c}}. \quad (19)$$

The value of l_c will be positive for the prograde case ($k = 1$) and negative for the retrograde case ($k = -1$) owing to the direction of spin of the black hole. The capture of a star can occur in two ways, either by tidal disruption of the stars or by direct capture by the black hole. For direct capture, we determine x_c using Equation (16) for $Q \neq 0$ or by using Equation (18) for $Q = 0$. Below a certain critical mass, the stars are tidally disrupted (Merritt 2013a) and above this the stars are swallowed whole. Therefore, r_t is defined as the radius below which the star gets disrupted by the black hole. We calculate the tidal radius in the presence of black hole spin applying Poisson's equation

$$\left. \frac{\partial^2 V_{eff}}{\partial r^2} \right|_{r=r_t} = -4\pi G\rho, \quad (20)$$

where ρ is the stellar mass density. Using the generalized form of the effective Kerr potential in natural units [Equation (14)], the tidal radius equation (Equation (20)), finally leads to

$$\left[-\frac{2}{x^3} + \frac{3(l^2 + Q)}{x^4} - 12 \frac{[(j-l)^2 + Q]}{x^5} - \frac{10j^3 Q}{x^6} \right]_{x=x_t} = -4\pi \tilde{\rho}, \quad (21)$$

where

$$\begin{aligned} \tilde{\rho} &= \frac{\rho}{M_\bullet} \cdot r_g^3 \simeq 0.3 M_8^2 \left(\frac{\rho_\star}{\rho_\odot} \right), \\ x &= r/r_g, \\ l &= L / \frac{GM_\bullet}{c}. \end{aligned} \quad (22)$$

where ρ_\star is the density of the star. We solve Equation (21) numerically for $x_t(j, k, M_8, Q)$ by considering $l = l_c$, the angular momentum of capture taking the above approximation for $\tilde{\rho} \simeq 0.3 M_8^2$ (assuming the star to be of solar type). An analytic approximation to r_t has been calculated in Appendix A.

The loss cone radius, $x_\ell \equiv \text{Max}[x_t, x_c]$ is given by

$$x_\ell(M_8, j, k, Q) = r_\ell/r_g = \text{Max}[r_t(M_8, j, k, Q), r_c(j, Q)]/r_g. \quad (23)$$

The angular momentum at x_ℓ is found by putting $V_{\text{eff}}(x, l, j, Q) = 0$ (see Equation (14)) to be

$$l_\ell(M_8, j, k, Q) = 2j + k \sqrt{\frac{2x_\ell j^2}{(x_\ell - 2)^2} - \frac{Q j^2}{x_\ell(x_\ell - 2)} + \frac{2x_\ell^2}{(x_\ell - 2)} - Q}. \quad (24)$$

The value of l_ℓ is positive for the prograde case ($k = 1$) and negative for the retrograde case ($k = -1$) owing to the direction of spin of the black hole. We show both the cases in Figure 4. For $Q = 0$ and $j = 0$, in the nonrelativistic limit (for high values of x_ℓ), using Equation (24), we obtain

$$L_\ell^2 = \left(\frac{GM_\bullet}{c}\right)^2 l_\ell^2 = \left(\frac{GM_\bullet}{c}\right)^2 2x_\ell = 2GM_\bullet r_\ell, \quad (25)$$

which is the well-known nonrelativistic result.

We show the variation of $x_\ell(M_8, j, k, Q)$ in Figure 3 (which is an input to the loss cone theory) and that of $x_t(M_8, j, k, Q)$ in Appendix A.

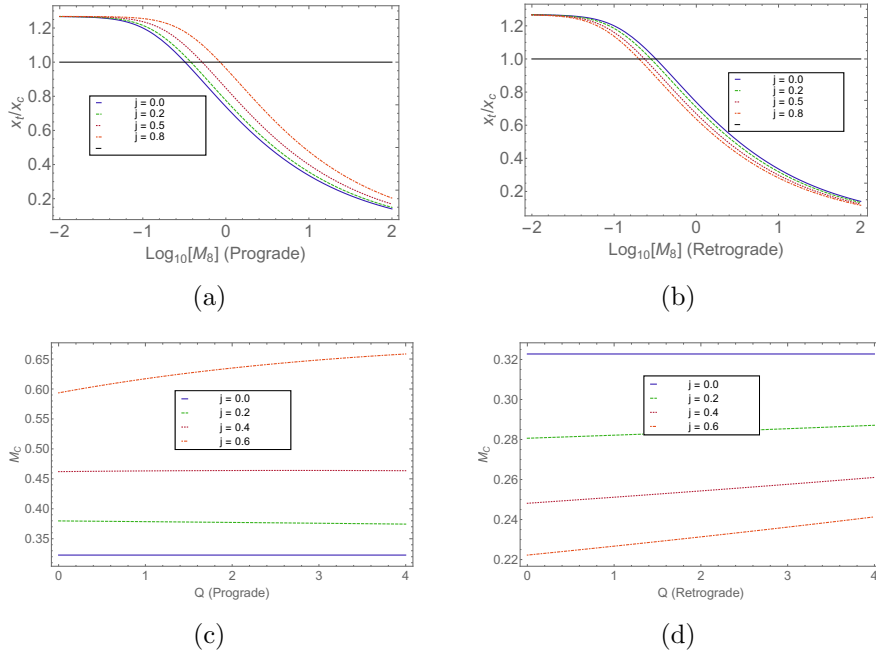


Figure 2. Ratio of tidal radius to the capture radius $[r_t(M_8, j, k, Q)/r_c(M_8, j, Q) = x_t(M_8, j, k, Q)/x_c(j, Q)]$ is shown as a function of M_8 for $Q = 0$ (a, b) and the locus of the critical mass, $M_c(j, Q)$ for different j as a function of Q (c, d). The critical mass of the black hole is determined from the plots when $x_t/x_c = 1$; this critical mass is represented by the black line in (a) and (b).

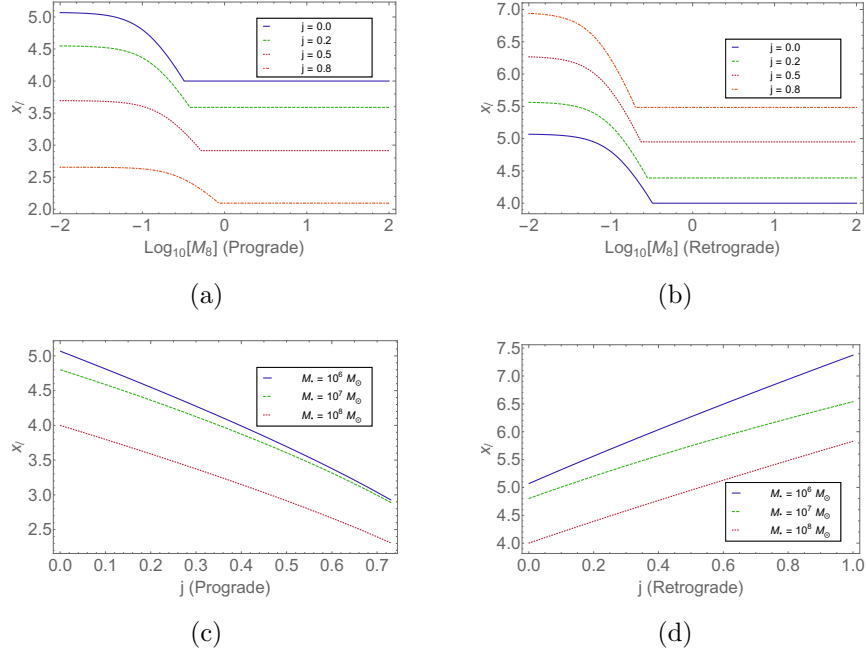


Figure 3. Loss cone radius ($x_\ell(M_8, j, k, Q) \equiv r_\ell(M_8, j, k, Q)/r_g = \text{Max}[x_t(M_8, j, k, Q), x_c(j, Q)]$) is shown as a function of M_8 (a, b) and j (c, d) for $Q = 0$.

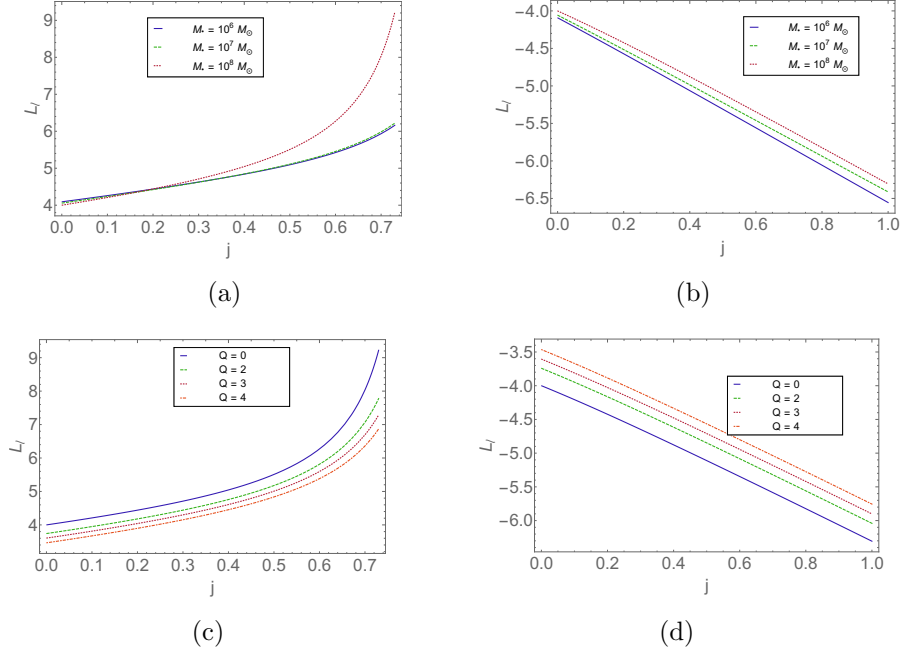


Figure 4. Loss cone angular momentum $l_\ell(M_8, j, k, Q)$ is shown as a function of j for $Q = 0$ (panels (a) and (b)) and different Q values with $M_8 = 1$ (panels (c) and (d)) for prograde (panels (a) and (c)) and retrograde (panels (b) and (d)) cases.

We explore the dependence of $M_c(j, Q)$, $r_t(M_8, j, k, Q)$ and $r_\ell(M_8, j, k, Q)$ in Figures 2, 18, 3 and 19 respectively. We observe the following:

1. Figure 2 shows the ratio $r_t(M_8, j, k, Q)/r_c(M_8, j, Q)$ as a function of both j and M_\bullet for $Q = 0$. $M_c(j, Q) = M_\bullet(r_t/r_c = 1)$ is the critical mass, which has a dependence on j and matches with the previous simulation results of Kesden (2012) who shows that the critical mass changes as a function of j , in the relativistic limit. For black holes more massive than $10^7 M_\odot$, but below the critical mass, the tidal disruption occurs very close to the horizon and Newtonian treatment of the tidal interactions cannot be applied. Kesden (2012) calculates equatorial ($Q = 0$) stellar orbits in the Kerr metric to evaluate the relativistic tidal tensor at the pericenter for the stars that are not directly captured by the black hole and also combine their relativistic treatment with previous calculations of the population of these orbits in order to determine tidal disruption rates for spinning black holes. They found a strong dependence of tidal disruption rates on black hole spin for $M_8 > 1$. Our calculation of r_t shows an increase at the high-mass end ($M_8 > 1$) as suggested by Kesden (2012). The bottom panels of Figure 2 show that $M_c(j, Q)$ is nearly flat in Q .
2. Figure 3 shows $x_\ell(M_8, j, k, Q)$ for $Q = 0$. When the value of $x_c(j, Q)$ exceeds $x_t(M_8, j, k, Q)$, the stars will be directly captured instead of getting tidally disrupted; hence, $x_\ell(M_8, j, Q)$ flattens out after $M_\bullet > M_c$. $x_\ell(M_8, j, k, Q)$ for different Q values are shown in Appendix A for both prograde and retrograde cases. For fixed j , in the retrograde case we see that $x_\ell(M_\bullet, j, k, Q)$ increases with Q and decreases with Q for the prograde case. $x_\ell(M_8, j, k, Q)$ for fixed M_\bullet is nearly the same for different Q . This is true because as Q increases, $L - L_z$ decreases, causing the pericenter to shrink in the prograde case, and the opposite occurs in the retrograde case.
3. The dimensionless angular momentum at $r_\ell(M_8, j, k, Q)$ defined as $l_\ell(M_8, j, k, Q)$ [Equation (24)] is the loss cone angular momentum in the relativistic regime. Fig 4 shows $l_\ell(M_8, j, k, Q)$ for different Q values, and it increases with M_8 for both prograde and retrograde cases for $Q = 0$. For fixed M_8 , $l_\ell(M_8, j, k, Q)$ decreases with an increase in Q for the prograde case, while it increases for the retrograde case. This can be understood from the fact that Q is a measure of $L - L_z$; so that L_z increases when Q decreases for $L_z > 0$ (prograde) and $|L_z|$ decreases when Q decreases for $L_z < 0$ (retrograde).

Steady loss cone theory: For typical masses $M_\bullet \gtrsim 10^5 M_\odot$, the more practical case is the steady-state theory of Cohn & Kulsrud (1978). By using direct numerical integration of the Fokker–Planck equation in angular momentum and energy space, they derived the stellar distribution in the presence of a black hole in a steady state. The distribution of orbital energies near the black hole can never reach a steady state because no black hole is old enough (Merritt 2013b), as expected for the distribution of orbital angular momenta near l_ℓ because $\tau_{M,*}/t_r \ll 1$ (see Appendix D, Table 2). Therefore, a hybrid approach should be used for the calculation of event rates based on the observed distribution of energies where the angular momentum distribution at each energy has reached an approximate steady state under the influence of gravitational encounters. We use the expression of the capture rate for full loss cone theory, \dot{N}_f , given by Merritt (2013b), and also derive the steady loss cone theory rate, \dot{N}_s . We discuss the conditions to determine which one is more appropriate. To see this, we examine the stellar capture in two situations, one where the loss cone gets filled quickly and another where it is dominated by diffusion. For the typical black hole mass under consideration (as $\frac{M_\bullet}{M_\odot}$ evolves from 10^4 to 10^8), the diffusive regime operates, and hence it is more appropriate to use the steady loss cone theory (see Appendix B for a detailed justification).

Mageshwaran & Mangalam (2015) (hereafter MM15) have constructed a detailed model of the tidal disruption events using stellar dynamical and gas dynamical inputs like black hole mass, specific orbital energy and also angular momentum, the mass of a single star, its radius, and the pericenter of the star orbit. Using the Cohn–Kulsrud boundary layer theory, they calculated the differential rate of number of stars falling in the steady loss cone to be (MM15)

$$\frac{d^2\dot{N}_s}{d\bar{e}dl^2dm} = 4\pi^2 s_t^{-1} \sigma^2 \xi(m) f_*(\bar{e}, M_\bullet, m) L_\ell^2(\bar{e}) F(\chi = 1, l), \quad (26)$$

where $s_t = r_t(M_\bullet, j)/r_h$, $\bar{e} = E/(GM_\bullet/r_t)$, E is the energy, f_* is the probability that a star of mass m is tidally captured as a main sequence, and $\xi(m)$ is the stellar mass function where $m = m_*/M_\odot$, $F = X(y_{lc})\zeta(q_s)$, and

$$X(y_{lc}) = \frac{f_s(E)}{1 + q_s^{-1} \zeta(q_s) \log(1/y_\ell)}, \quad (27)$$

with $q_s = \frac{\langle D(E) \rangle}{y_\ell}$ and $y_\ell = \frac{L_\ell^2}{J_c^2}$ where $f_s(E)$ is the distribution function of stars in the galaxy. $\langle D(E) \rangle$ is the orbit-averaged angular momentum diffusion coefficient, and J_c is the angular momentum of circular orbit. MM15 have used the M_\bullet - σ relation (taking $p = 4.86$) to get the expression for \dot{N}_s . By applying the steady-state Fokker-Planck equation while using a power-law stellar density profile (having power-law index γ), they obtained the rate of capture of stars $\dot{N} \propto M_\bullet^\beta$, where $\beta = -0.3 \pm 0.01$ for $M_6 > 10$ and the value of \dot{N}_s is $\sim 6.8 \times 10^{-5} \text{ yr}^{-1}$ for $\gamma = 0.7$. We apply the same technique to calculate \dot{N}_s , including the relativistic forms of r_t and r_c , but do not assume the M_\bullet - σ relation a priori and consider σ as an independent parameter in our model. We start from the basic equation for N_s given by

$$N_s = 4\pi^2 \int P(E) dE \int f_s(E, J) dJ^2, \quad (28)$$

where $P(E)$ is the orbital period. We use the same expressions and parameters given in MM15 with the following assumptions:

$$\int \xi(m) dm = 1, \quad f_* = 1, \quad (29)$$

and

$$\langle D(\epsilon_s) \rangle = \frac{32\sqrt{2} \pi^2 G^2 \langle m_f^2 \rangle \log \Lambda}{3 J_c^2} \frac{M_\bullet}{\langle m_* \rangle \sigma^2} [2h_1(\epsilon_s) + 3h_2(\epsilon_s) - h_3(\epsilon_s)], \quad (30)$$

where m_f is the mass of the field star, with the maximum mass taken to be $150 M_\odot$, $\Lambda \approx M_\bullet/m_*$, $\epsilon_s = E/\sigma^2$, and h_1 , h_2 and h_3 are defined in MM15. Now,

$$J_c^2 = \sigma^2 r_h^2 [s_c(\epsilon_s) + 2s_c^{4-\gamma}(\epsilon_s)], \quad (31)$$

where s_c is the ratio of the radius of circular orbit and the horizon radius, the ϵ_s -dependent part is called as $\beta(\epsilon_s)$, and

$$L_\ell(M_\bullet, j, k, Q) = \frac{GM_\bullet}{c} l_\ell(M_\bullet, j, k, Q). \quad (32)$$

Therefore,

$$y_\ell(M_\bullet, j, k, Q, \epsilon_s) = \frac{L_\ell^2}{J_c^2} = \frac{L_\ell^2(M_\bullet, j, k, Q)}{\sigma^2 r_h^2 \beta(\epsilon_s)}, \quad (33)$$

where $\beta(\epsilon) = [s_c(\epsilon_s) + 2s_c^{4-\gamma}(\epsilon_s)]$. From the definition, $q_s(\epsilon_s)$ is written as

$$q_s(\epsilon_s) = \frac{\langle D(\epsilon_s) \rangle}{y_\ell}, \quad (34)$$

which can be simplified to

$$q_s(M_\bullet, j, k, Q, \epsilon_s, \sigma) = \frac{32\sqrt{2}}{3} \frac{\pi^2 \langle m_f^2 \rangle}{M_\bullet \langle m_* \rangle} \frac{\log \Lambda \sigma^2 r_h^2}{L_\ell^2(M_\bullet, j, k, Q)} [2h_1(\epsilon_s) + 3h_2(\epsilon_s) - h_3(\epsilon_s)]. \quad (35)$$

The expression $\zeta(q_s)$, as given by MM15 is

$$\zeta(q_s) = \begin{cases} 1 & \text{for } q_s \geq 4 \\ q_s / (0.86q_s^{0.5} + 0.384q_s - 0379q_s^{1.5} + 0.427q_s^2 - 0.095q_s^{2.5}) & \text{otherwise.} \end{cases} \quad (36)$$

By integrating Equation (26) assuming $f_* = 1$, we finally arrive at

$$\frac{dN_s}{d\epsilon_s}(M_\bullet, j, k, Q, \epsilon_s, \sigma) = \frac{\sqrt{2}\pi^3 L_\ell^2(M_\bullet, j, k, Q) \sigma^2 \epsilon_s^{-\frac{3}{2}}}{G^2 M_\bullet \langle m_* \rangle} g(\epsilon_s) \frac{\zeta(q_s)}{1 + q_s^{-1} \zeta(q_s) \log(1/y_\ell)}. \quad (37)$$

Then, dividing Equation (37) by the orbital period $P(\epsilon_s)$, we find an expression of $\frac{d\dot{N}_s}{d\epsilon_s}$ as

$$\frac{d\dot{N}_s}{d\epsilon_s}(M_\bullet, j, k, Q, \epsilon_s, \sigma) = \frac{4\pi^2 L_\ell^2(M_\bullet, j, k, Q) \sigma^5}{G^3 M_\bullet^2 \langle m_* \rangle} g(\epsilon_s) \frac{\zeta(q_s)}{1 + q_s^{-1} \zeta(q_s) \log(1/y_\ell)}, \quad (38)$$

where we have used the relativistic approximation to $r_\ell(M_\bullet, j, Q)$ to obtain $\dot{N}_s(M_\bullet, j, k, Q, \epsilon_s, \sigma)$ in the relativistic limit as a function of the black hole spin. Since the diffusion occurs at very large radius, only the first term of the effective potential dominates. Integrating this expression numerically, we finally find the rate of capture of stars for the case of the steady loss cone, and Figure 5 shows the resulting variation of $\dot{N}_s(M_\bullet, j, k, Q, \epsilon_s, \sigma)$ with the M_\bullet . $\dot{N}_s(M_\bullet, j, k, Q, \epsilon_s, \sigma)$ has very little dependence on Q ; our results for $Q = 4$ are similar to Figure 5 for $Q = 0$. Therefore, $\dot{N}_s(M_\bullet, j, k, Q, \epsilon_s, \sigma)$ is nearly independent of the value of Q .

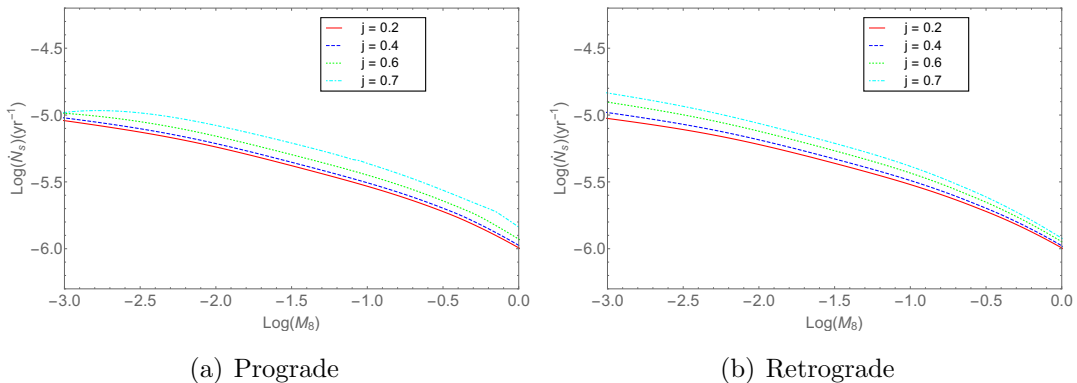


Figure 5. Capture rate, $\dot{N}_s(M_\bullet, j, k, Q, \epsilon_s, \sigma)$, is shown which reduces monotonically with M_8 and increases slightly with j when $k = 1$ (panel (a)) and -1 (panel (b)) for $Q = 0$, where the lower limit of the ϵ_s integration is taken to be $\epsilon_m = -10$, $\gamma = 1.1$, and $\sigma = 200 \text{ km s}^{-1}$.

The monotonic decrease of \dot{N}_s can be explained by the decrease of l_ℓ with M_8 . From Figure 5, we see that $\dot{N}_s(M_\bullet, j, k, Q, \epsilon_s, \sigma)$ increases with an increase in j . When we apply the M_\bullet - σ relation taking $p = 4.86$, we find that the capture rate, $\dot{N}_s(M_\bullet, j, k, Q, \epsilon_s, \sigma)$ (see Figure 21), follows a similar trend to that of Kesden (2012) (see Figures 3, 4), where $\dot{N}_s(j)$ increases with j with the assumption of the universal M_\bullet - σ relation. For higher γ , \dot{N}_s increases for both the prograde and retrograde cases, which is similar to the result of MM15. The difference between the full and steady loss cone capture rates is discussed in Appendix C. We derive the mass evolution only in the presence of stellar capture, and the result obtained is in rough agreement with that of Alexander & Bar-Or (2017).

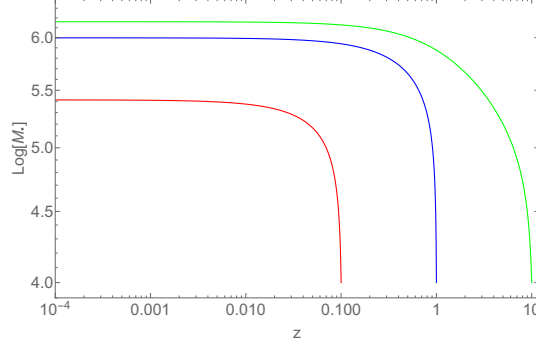


Figure 6. Mass evolution only in the presence of stellar capture is shown for a seed mass of $10^4 M_\odot$, $\gamma = 1.1$, and at different formation redshifts (red is for $z_f = 0.1$, blue is for $z_f = 1$, green is for $z_f = 10$).

Figure 6 is similar to the result of Alexander & Bar-Or (2017) [see Figure 2] under the same conditions.

2.3. Growth of the Black Hole by Mergers

The black holes can grow their mass also by the merger process, though the rate is generally much smaller compared to accretion, while minor mergers are more probable than the major mergers. When the accretion process stops owing to saturation, the dominant contribution to mass growth of the black hole comes from the effect of mergers. We compute the mass growth rate by merger activity by integrating the merger rate over the mass of the smaller black hole. Stewart et al. (2009) use high-resolution Λ CDM N -body simulations for predicting merger rates in dark matter halos and investigate the scaling of common merger-related observables with luminosity, stellar mass, merger mass ratio, and redshift $z = 4 \rightarrow 0$. They derive the expression for merger rate (infall) valid for $0 \leq z \lesssim 4$ considering the peak of merger activity; the dependence on different parameters has been determined using simple fitting functions. They developed simulations that contained 512 particles of mass $3.16 \times 10^8 h^{-1} M_\odot$ which was evolved within a comoving volume of $80 h^{-1}$ Mpc on a side by the Adaptive Refinement Tree (ART) N -body code developed by Kravtsov et al. (1997, 2004). We use the rate of mergers given in Stewart et al. (2009) and integrate it over the mass of the smaller black hole to find $\dot{M}_{\bullet m}$. Following their assumptions, we also consider the merger activity to be valid in the range $z = 4 \rightarrow 0$. In Stewart et al. (2009) the empirical expression for merger rate (infall) is

$$\frac{dN_m}{dt}(m/M \in (0.1, 0.7)) = A_t(z, M)F(m/M), \quad (39)$$

where m and M are the masses of the smaller and larger merging galaxies and N_m is the number of mergers,

$$A_t(z, M) = 0.02 \text{Gyr}^{-1} (1+z)^{2.2} M_{12}^b, \quad (40)$$

with $b = 0.15$ and $M_{12} = M / 10^{12} h^{-1} M_\odot$ with $h = 0.7$ that is valid for $0 \leq z \lesssim 4$. Adopting this, the rate of mass growth due to mergers is given as

$$\frac{dM}{dt} = A_t M \int_q^1 F(q) dq = A_t M n(q), \quad (41)$$

where $q = m/M$, and $F(q)$ is given as

$$F(q) = q^{-c} (1-q)^d, \quad (42)$$

where $c = 0.5$ and $d = 1.3$ and $n(q)$ can be written as a combination of complete and incomplete Beta functions, where the complete and incomplete Beta functions are defined, respectively, as

$$B(x, y) \equiv \int_0^1 t^{x-1} (1-t)^{y-1} dt, \quad (43)$$

and

$$B_z(x, y) = \int_0^z t^{x-1} (1-t)^{y-1} dt \equiv \frac{z^x}{x} {}_2F_1(x, 1-y; x+1; z) \quad (44)$$

As a result, we can express

$$n(q) = B(1-c, 1+d) - B_q(1-c, 1+d), \quad (45)$$

so that the merger mass rate becomes

$$\dot{M}_{\bullet m} = 8.058 \times 10^{-3} (1+z)^{2.2} \left[\frac{M_5}{f_h} \right]^{1.15} n(q) M_5 \cdot 10^5 M_\odot / \text{Gyr}; \quad (46)$$

In units where $\mu_\bullet = \frac{M_\bullet}{M_s}$, where M_s is the seed mass, $\tau = \frac{t}{t_0}$, where $t_0 = 1$ Gyr, this can further be expressed as

$$\dot{\mu}_m(q, M_s, z, z_f) = \frac{\dot{M}_{\bullet m} t_0}{M_s} = \frac{8.058 \times 10^{-3} (1+z)^{2.2} \left[\frac{M_5}{f_h} \right]^{1.15} n(q) M_5}{M_{s5}}, \quad (47)$$

where $f_h = M_\bullet/M$ and M_5 is the mass of the SMBH in units of $10^5 M_\odot$ which simplifies to

$$M_{\bullet 5}(q, M_s, z, z_f) = \left[M_{s5}^{0.15} - 1.21 \times 10^{-3} \int_{z_f}^z (1+z)^{2.2} n(q) \frac{dt}{dz}(z) \right]^{-\frac{20}{3}}, \quad (48)$$

where we have used $f_h = 3 \times 10^{-5}$, $\frac{dt}{dz}$ is given by Equation (70), and z_f is the formation redshift. For simplicity, we assume a proportionality relation, $M_\bullet = f_h M$, while Ferrarese (2002) and Jahnke & Macciò (2011) have assumed the relation to be slightly nonlinear, with the index of the relation

dependent on the choice of the dark matter profile. Furthermore, f_h increases to 2×10^{-4} for halo masses of $\sim 10^{14} M_\odot$ and decreases to 10^{-5} for halo masses of $\sim 10^{12} M_\odot$ (Ferrarese 2002). Therefore, as a reasonable approximation, we assume a mean value of f_h in our model. The frequency of major mergers is much less than the frequency of minor ones (Stewart et al. 2009). Gammie et al. (2004) consider the collapse of stars, accretion, and major and minor mergers that contribute to the spin of the astrophysical black holes. Major mergers contribute to spinning up the hole, whereas minor mergers contribute to spinning it down (Gammie et al. 2004). Since accretion is dominant for spinning up of the black hole, we consider only the contribution of minor mergers for spin-down and neglect the major mergers for the spin evolution of the hole in our model. Different models suggest that black holes produced by the collapse of a supermassive star are likely to have $j \sim 0.7$. Though the result of major mergers is not yet known, Gammie et al. (2004) provide some current estimates and analytic bounds on j for these processes. They apply the formalism of Hughes & Blandford (2003) to minor mergers assuming an isotropic distribution of orbital angular momentum and find that the spin-down occurs with $j \sim M^{7/3}$ and evaluate a power law for spin decay for the limit of the small value of j , by expanding the radius and specific energy of ISCO as a function of j . Their simulations for accretion process from fully relativistic MHD flow indicates a spin equilibrium at $j \sim 0.9$, much less than the canonical value 0.998 of Thorne (1974) that was derived excluding the MHD effects. This suggests the possibility that the black holes that grow mainly by the accretion process are not maximally rotating. We use the spin-down term by minor mergers given by Gammie et al. (2004) in our evolution model to be valid in the range $z = 4 \rightarrow 0$, which causes a significant decrease in the final spin value. Gammie et al. (2004), by taking the effect of minor mergers on spin evolution of the black hole, find

$$\frac{d \log j}{d \log M_\bullet} = -\frac{7}{3} + \frac{9q}{\sqrt{2}j^2}, \quad (49)$$

which can be written as

$$\frac{dj}{d\tau} = \dot{\mu}_m \cdot \frac{j}{\mu_\bullet} \left(-\frac{7}{3} + \frac{9q}{\sqrt{2}j^2} \right). \quad (50)$$

The merger term dominates after the accretion stops, which happens after the black hole reaches saturation. We have used $q = 0.1$, as $q > 0.1$ implies major mergers. But the frequency of major mergers is much less than the minor ones, and the growth rate by major mergers is almost of the same order for different q values. We see that the mass growth due to mergers is significantly smaller in this case compared to the gas accretion, and hence we consider only the minor mergers, as they are more frequent.

2.4. Recipe for the Electromagnetic Spin-down of the Black Hole

If magnetic field lines are present in a rotating black hole supported by external currents that are flowing in an equatorial disk, there will be an induced electrical potential difference. For large field strengths, the vacuum will be unstable to the cascade production of an electron–positron pair creating a force-free magnetosphere, leading to an electromagnetic extraction of energy and angular momentum. Blandford & Znajek (1977) have derived an approximate solution for spinning black holes to provide a model of the central engine of the AGN. The advantage of this model is that the relativistic electrons can be accelerated efficiently compared to other models. We include the BZ effect for causing the spin-down of the hole in our model. The spin-down due to BZ torque is implemented

by Equation (14) in [Mangalam et al. \(2009\)](#), where they study the case of rapid loss of cold gas due to AGN feedback, which may cause expansion in the effective radii of massive elliptical galaxies from $z \simeq 2$ to 0; they quantify the extent of the expansion in terms of the star formation parameters and time of the expulsion of the cold gas; and they show that cosmological changes are expected to have a major influence on the gas accretion mode, which at high redshifts can be dominantly cold thin disk accretion and at low redshifts could be dominantly hot Bondi-fed ADAF accretion. They calculate the spin-down to be $\tau_j \sim M_9^2 0.2$ Gyr, which explains the cosmological evolution of the luminosity function from powerful to weak radio galaxies. We use the expression of spin evolution caused by BZ torque as implemented in [Mangalam et al. \(2009\)](#) in our model. We calculate the spin evolution by the BZ effect for different initial and final spin values ([Mangalam et al. 2009](#)) from

$$\frac{dj}{dt} = x_+^3(j)j \frac{\mathcal{G}_0}{\mathcal{J}_0}, \quad (51)$$

where $x_+(j) = 1 + \sqrt{1 - j^2}$ and the BZ torque, \mathcal{G}_0 , is given by

$$\mathcal{G}_0 = \frac{m^3}{8} B_\perp^2 f_{BZ} = 4 \times 10^{46} f_{BZ} B_4 M_8^3 (\text{erg}), \quad (52)$$

and the angular momentum budget, \mathcal{J}_0 is

$$\mathcal{J}_0 = cM_\bullet m = 9 \times 10^{64} M_8^2 (\text{g cm}^2 \text{ s}^{-1}), \quad (53)$$

and where $B_4 = B/10^4 \text{Gauss}$, f_{BZ} is a geometric factor that comes from the averaging of the angle over the horizon of magnetic flux and the spin of the magnetic field ([Mangalam et al. 2009](#)). Therefore, in dimensionless form

$$\frac{dj}{d\tau} = \frac{4}{9} \times 10^{-5} f_{BZ} B_4 \mu_\bullet M_{s5} x_+^3(j)j, \quad (54)$$

whose analytic solution of spin-down time $\tau_{j,BZ}(j)$ is given by ([Mangalam et al. 2009](#))

$$\tau_{j,BZ} = \frac{\mathcal{J}_0}{\mathcal{G}_0} \int_{j_f}^{j_i} \frac{dj}{r^3(j)j} = 7.0 \times 10^8 \text{yr} \frac{(\kappa(j_i, j_f)/0.1)}{B_4^2 M_9 f_{BZ}}, \quad (55)$$

where $M_9 = M_\bullet/(10^9 M_\odot)$ and

$$\kappa(j_i, j_f) = \left[\left(\frac{1}{16} \right) \log \left(\frac{2-w}{w} \right) + \left(\frac{3w^2 + 3w - 4}{24w^3} \right) \right]_{w_f}^{w_i}, \quad (56)$$

with $w_i = x_+(j_i)$, $w_f = x_+(j_f)$. This is equivalent to the study of the spin-down for the Bondi case with zero accretion in [Mangalam \(2015\)](#).

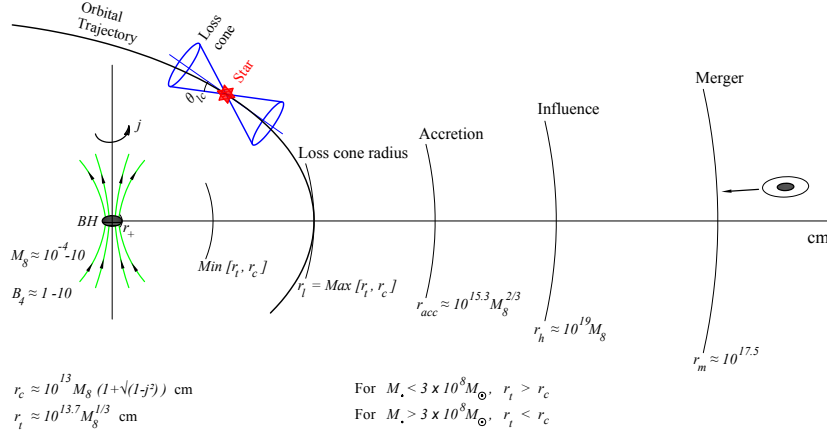


Figure 7. Important radii corresponding to all the processes contributing to the growth of the black hole is shown for $M_\bullet = 10^4 - 10^6 M_\odot$.

Effects	Region	τ_j	τ_M
Gas accretion	$r_I - r_d$	1 Gyr	1 Gyr
Stellar capture	$r_t - r_h$	-	10 Gyr
Mergers	r_M	10 Gyr	~ 10 Gyr
BZ torque	$r_+ - r_I$	1 Gyr	-

Table 2. The Domain and Timescales for Different Physical Effects (Shown in Figure 7) Contributing to the Growth of the Black Hole.

We indicate operative time scales in different physical regimes of gas accretion, stellar capture, mergers, and electromagnetic torque in Table 2, where the evolution timescales for mass, τ_M , and spin, τ_j , are calculated in Appendix D. It is clear that the evolution timescales of both mass and spin are of order 1–10 Gyr. This motivates us to use $t_0 = 1$ Gyr as the unit of time in our model.

3. BLACK HOLE EVOLUTION MODEL IN Λ CDM COSMOLOGY

The black hole growth can occur by gas flow and by capture of stars and mergers until it reaches a saturated mass $M_{\bullet t}$ at a time $t = t_s$ when the gas flow stops and it grows only by the capture of stars and mergers. This happens because the outflow velocity exceeds the escape velocity of the medium and the gas is driven away, causing the accretion process to stop. The saturated mass is given by King (2003) as

$$M_{\bullet t} = 9.375 \times 10^6 \sigma_{100}^4 M_\odot. \quad (57)$$

For the rate of growth of mass by mergers, we use Equation (41), which is valid from $z = 4$ to the present time, given that the merger activity peaks at $z = 5-0.5$ (Wetzel et al. 2009). We perform five experiments that we discuss in this section. For the mass evolution, we consider the contribution from both major mergers and the minor ones, and for the spin evolution, we consider only the contribution from the minor mergers to spinning down the black hole (Gammie et al. 2004), as the contribution of the accretion process in spinning up the black hole is much higher than the contributions from mergers. But due to a smaller frequency of the major mergers, the final mass attained by the merger process does not vary significantly with the value of q . We have dealt with two scenarios: (i) for $z_f \lesssim 4$ the contribution of the mergers will be present throughout; and (ii) for $z_f \gtrsim 4$, initially, there will be only accretion and stellar capture, and mergers will come into play later than $z = 4$; from then on until t_s , all the three terms will contribute, after which the accretion stops.

To summarize, our model is based on some assumptions and conditions:

1. Black hole seeds are formed at look-back times of the order of the Hubble time.
2. At the saturation time, the mass reaches $M_{\bullet t} = 9.375 \times 10^6 \sigma_{100}^4 M_\odot$ and $p \rightarrow 4$.
3. The merger activity exists only for $z \lesssim 4$ (Stewart et al. 2009).

As before, we have normalized mass by $\mu_\bullet = \frac{M_\bullet}{M_s}$, where M_s is the seed mass, and time by $\tau = \frac{t}{t_0}$, where $t_0 = 1$ Gyr. The mass evolution equation is given by Equation (3) as

$$\frac{dM_\bullet}{dt} = \epsilon_I(j)\dot{M}_{\bullet g} + \epsilon(j)\dot{M}_{\bullet*} + \dot{M}_{\bullet m}, \quad (58)$$

where $\epsilon(j)$ is the mass accretion efficiency given by

$$\epsilon(j) = \begin{cases} \epsilon_I(j) & \text{for } M_\bullet < M_c \\ 1 & \text{for } M_\bullet \geq M_c, \end{cases} \quad (59)$$

where (Bardeen et al. 1972)

$$\epsilon_I(j) = \frac{z_m^2(j) - 2z_m(j) + j\sqrt{z_m(j)}}{z_m(j)(z_m^2(j) - 3z_m(j) + 2j\sqrt{z_m(j)})^{1/2}}, \quad (60)$$

and

$$z_m(j) = \frac{r_{ms}}{M_\bullet} = 3 + Z_2 - k\sqrt{(3 - Z_1)(3 + Z_1 + 2Z_2)}, \quad (61)$$

with $Z_1 = 1 + (1 - j^2)^{1/3}((1 + j)^{1/3} + (1 - j)^{1/3})$ and $Z_2 = (3j^2 + Z_1^2)^{1/2}$ (Bardeen et al. 1972). The dimensionless equation becomes

$$\frac{d\mu_\bullet}{d\tau} = \epsilon_I(j)\dot{\mu}_g + \epsilon(j)\dot{\mu}_* + \dot{\mu}_m. \quad (62)$$

The first term on the right-hand side of Equation (62) represents the gas accretion and stems from Equation (11), the second term due to the stellar capture is calculated from Equation (38) and represented below by Equation (66), and the third term comes from the contribution of mergers

provided by Equation (47). In Equation (59), we see that $\epsilon(j)$ is given by efficiency at ISCO for $M_\bullet < M_c$ and 1 for $M_\bullet > M_c$. This is because, beyond the critical mass, the stars are directly captured with the efficiency of 1, while for $M_\bullet < M_c$, the gas enters through ISCO (by accretion of tidally disrupted stars) with efficiency, ϵ_I . The gas accretion is through ISCO, but, the stars can disrupt and enter by gas accretion through ISCO, as well as by direct capture.

The spin evolution equation of black holes taking into account gas accretion, stellar capture, mergers, and BZ torque is given by Equation (4) as (see §2 for the various terms)

$$\frac{dj}{dt} = \frac{\dot{M}_{\bullet g}}{M_\bullet} \left(l_I(j) - 2\epsilon_I(j)j \right) + \frac{\dot{M}_{\bullet*}}{M_\bullet} \left(l_*(j) - 2\epsilon(j)j \right) + \dot{M}_{\bullet m} \cdot \frac{j}{M_\bullet} \left(-\frac{7}{3} + \frac{9q}{\sqrt{2}j^2} \right) + x_+^3(j)j \frac{\mathcal{G}_0}{\mathcal{J}_0}. \quad (63)$$

The dimensionless version of Equation (63) is

$$\frac{dj}{d\tau} = \frac{\dot{\mu}_g}{\mu_\bullet} \left(l_I(j) - 2\epsilon_I(j)j \right) + \frac{\dot{\mu}_*}{\mu_\bullet} \left(l_*(j) - 2\epsilon(j)j \right) + \dot{\mu}_m \cdot \frac{j}{\mu_\bullet} \left(-\frac{7}{3} + \frac{9q}{\sqrt{2}j^2} \right) + \frac{4}{9} \times 10^{-5} f_{BZ} B_4 \mu_\bullet M_{s5} x_+^3(j)j. \quad (64)$$

where

$$\dot{\mu}_g(M_\bullet, M_s) = \begin{cases} \frac{\dot{M}_{\bullet g} t_0}{M_s} = \frac{k_1 M_{\bullet t} t_0}{M_s} & \text{for } M_\bullet \leq M_{\bullet t}; \quad k_1 = \frac{4\pi G m_p \eta}{\sigma_e c} \\ 0 & \text{for } M_\bullet > M_{\bullet t}, \end{cases} \quad (65)$$

$$\dot{\mu}_*(M_\bullet, j, k, Q, \epsilon_s, \sigma, M_s) = \frac{\dot{M}_{\bullet*} t_0}{M_s} = \begin{cases} m_* \dot{N}_f t_0 / M_s & \text{for full loss cone} \\ m_* \dot{N}_s t_0 / M_s & \text{for steady loss cone} \end{cases}, \quad (66)$$

where \dot{N}_f and \dot{N}_s are the stellar capture rates derived for full or steady loss cone theories. We define

$$\dot{\mu}_m(M_\bullet, q, M_s, z, z_f) = \begin{cases} \frac{\dot{M}_{\bullet m} t_0}{M_s} & \text{for } z \leq 4, \\ 0 & \text{for } z > 4 \end{cases}, \quad (67)$$

where M_{s5} is the mass of the seed black hole in units of $10^5 M_\odot$; for our calculations we have used $f_{BZ} = 1$. The first term on the right-hand side of Equation (64) for gas accretion stems from Equation (12) [which shuts off after saturation, as implemented in Equation (65)]. The second term represents the stellar capture, which can happen in two ways: by tidal disruption (for $M_\bullet < M_c$) when the gas has to pass through ISCO with an angular momentum and efficiency at ISCO, or by a direct capture (for $M_\bullet > M_c$), when it will retain its original angular momentum and efficiency, $\epsilon(j) = 1$ as given by Equations (59) and (68). The third term represents mergers and stems from Equation (50) (effective during $z = 4 \rightarrow 0$; see (4) in our assumptions as implemented in Equation (67)), and the last term represents the contribution of BZ torque (see Equation (54)). The angular momentum of the stellar component is given by

$$l_*(M_\bullet, j, k, Q) = \begin{cases} l_I(j) = \frac{z_m^2(j) - 2j\sqrt{z_m(j)} + j^2}{z_m^{1/2}(j)[z_m^2(j) + 2j\sqrt{z_m(j)} - 3z_m(j)]^{1/2}} & \text{for } M_\bullet < M_c(j) \\ l_\ell(M_\bullet, j, k, Q) = 2j + k\sqrt{\frac{2x_\ell j^2}{(x_\ell - 2)^2} - \frac{Qj^2}{x_\ell(x_\ell - 2)} + \frac{2x_\ell^2}{(x_\ell - 2)}} - Q & \text{for } M_\bullet \geq M_c(j), \end{cases} \quad (68)$$

where $l_I(j)$ is given by Equation (E16) (Bardeen et al. 1972) and $l_\ell(M_\bullet, j, k, Q)$ is given by Equation (24). which depends on $x_\ell(M_\bullet, j, k, Q)$. If we take $\{j = 0, Q = 0\}$, we obtain the nonrelativistic result from the expression of $L_\ell(M_\bullet, j, k, Q) = l_\ell \frac{GM_\bullet}{c}$, as shown in Equation (25). For Λ CDM cosmology, we take $\Omega_r = 0$, $\Omega_m = 0.3$, $\Omega_\Lambda = 0.7$, and the look-back time as a function of redshift can be written as

$$t(z) = \frac{1}{H_0} \int_{1/(1+z_f)}^{1/(1+z)} da \frac{1}{\sqrt{\Omega_m a^{-1} + \Omega_\Lambda a^2}} = t_z(z) - t_z(z_f), \quad (69)$$

where z_f is the formation redshift and H_0 is the present-day Hubble constant ($H_0 = 70 \text{ km s}^{-1} \text{ Mpc}^{-1}$), and where we find by direct integration that

$$t_z(z) = \frac{1}{H_0} \frac{2}{3} \frac{1}{\sqrt{1 - \Omega_m}} \log \left[\sqrt{1 - \Omega_m} \sqrt{\Omega_m + \frac{1 - \Omega_m}{(1+z)^3}} + (1 - \Omega_m) \left(\frac{1}{1+z} \right)^{\frac{3}{2}} \right]. \quad (70)$$

which matches with the result of Mo et al. (2010) for $z_f = \infty$. The boundary conditions are

1. At $t = 0$, $M_\bullet = M_s$, $z = z_f$ and $j = j_0$.

2. At $t = t_s$, $M_\bullet = M_{\bullet t}$, $z = z_s$.

Equations (58) and (63) are the basic evolution equations of the black hole mass and spin that we solve along with all the auxiliary equations (Equations (59–62), (64–70)).

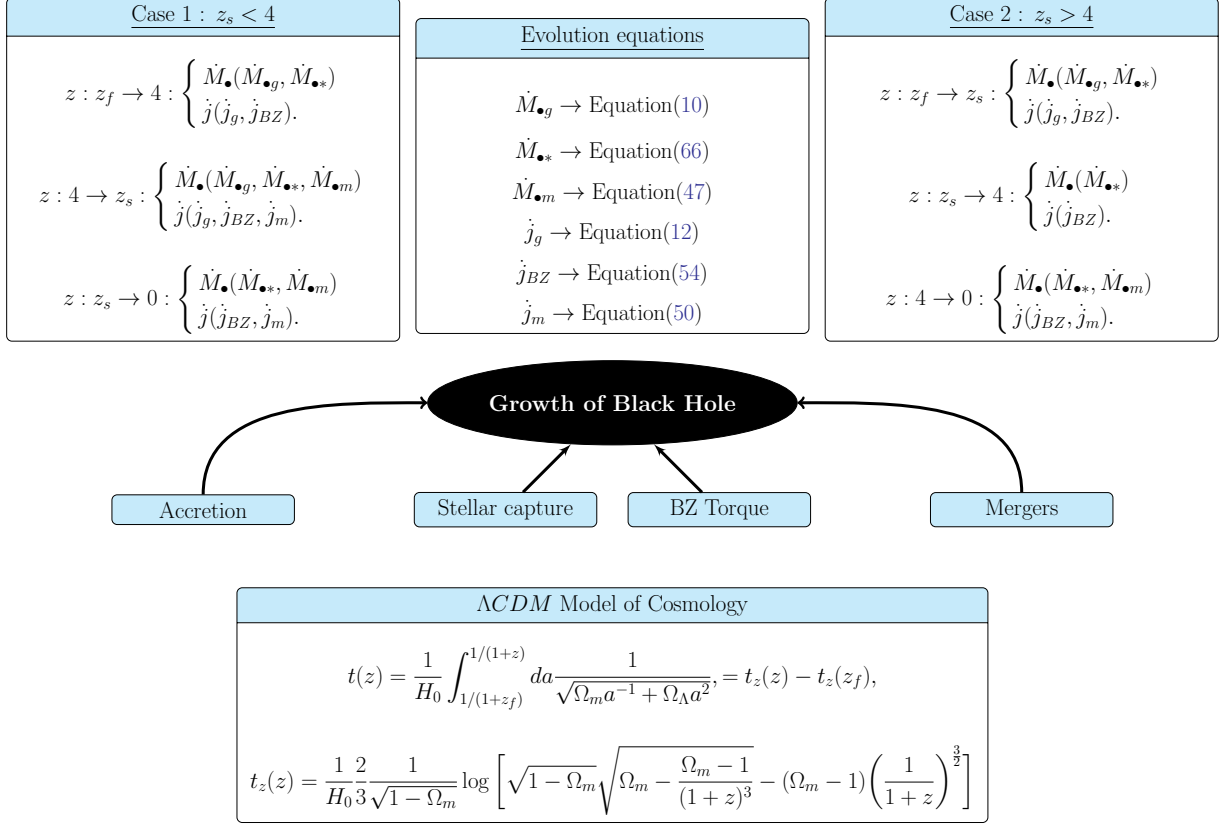


Figure 8. A schematic for our model of evolution of the mass and the spin of black hole in Λ CDM cosmology.

We perform the following experiments, which we tabulate in Table 3. Next, we discuss the parameter range.

Models	Accretion	BZ Torque	Stellar Capture	Mergers	Parameter Sets
Expt 1	✓				M_s, η, j_0, z_f
Expt 2	✓		(FLC)✓		$M_s, \eta, j_0, z_f, \sigma_{100}$
Expt 3	✓	✓			M_s, η, j_0, z_f, B_4
Expt 4	✓	✓	(SLC)✓		$M_s, \eta, j_0, z_f, \sigma_{100}$
Complete model	✓	✓	(SLC)✓	✓	$M_s, \eta, j_0, z_f, \sigma_{100}, q$

Table 3. Description of the Five Different Experiments Performed for Various Combinations of Astrophysical Components Included, along with the Parameter Sets.

Justification of the chosen parameter ranges: To perform the experiments given in Table 3, we choose the ranges of the input parameters, which are justified by observational values. The minimum σ measured to date is around 30 - 40 km s⁻¹ (Xiao et al. 2011). For this low σ , the saturated mass is of the order of around $10^5 M_\odot$. Therefore, the seed masses considered should be $\lesssim 10^5 M_\odot$.

The ranges we consider for seed mass and formation redshift are consistent with the values considered by [Alexander & Bar-Or \(2017\)](#). The values of z_f are taken to be in the range $z_f = 5-8$. Average observed values of σ are within the range of 100–200 km s⁻¹. Values of $\gamma \simeq 1.1-1.5$ are consistent with the observed values ([Merritt 2013a](#)). The B_4 values are taken to be in the typical range of 1-10 ([Blandford et al. 1990](#)), for a black hole of mass $10^8-10^{10} M_\odot$; [Blandford & Znajek \(1977\)](#) show that the field strength should be more than 10^5 G for supplying electromagnetic power equal to or more than the Eddington power. The η values are typically sub-Eddington ($\eta \gtrsim 0.07$), and below that it will not be possible to attain the high mass of the present-day black holes. We have used η in the range [0.07, 0.09] as given in [Shankar et al. \(2009b\)](#), including the effect of duty cycles. We have also illustrated the case of $\eta = 0.01$, which clearly indicates a very slow mass growth.

Parameters	Ranges	References
$M_{\bullet s}$	$10^3 - 10^5 M_\odot$	Alexander & Bar-Or (2017)
j_0	0.001 - 0.4	Mangalam (2015)
z_f	5 - 8	Alexander & Bar-Or (2017)
η	0.07 - 0.09	Shankar et al. (2009b)
σ_{100}	1 - 2.5	(Xiao et al. 2011), Bhattacharyya & Mangalam (2018)
γ	1.1 - 1.5	Merritt (2013a)
B_4	1 - 10	Blandford et al. (1990)

Table 4. The Ranges of the Parameters Used in Our Model Are Shown and Are Based on the Papers Cited.

Run #	$M_s(10^5 M_\odot)$	B_4	σ_{100}	z_f	η	j_0	Varying Parameter	Comments
1.1	1	5		4	0.09	0.001	$j_0 = 0$	Expt 1
1.2	1	10		4	0.09	0.2		
2.1.	0.1		1	10	0.09		M_s	Expt 2
2.2	0.5		1	10	0.09			
2.3	1		1	10	0.09			
3.1.1	1	1		4	0.09	0.2	B_4	Expt 3.1
3.1.2	1	5		4	0.09	0.2		
3.1.3	1	10		4	0.09	0.2		
3.2.1	1	5		4	0.01	0.2	Lower limit of η	Expt 3.2
3.2.2	1	5		4	0.05	0.2		
4.1.1	0.5	5	1	6	0.07	0.2	M_s	Expt 4.1 /Expt 5.1*
4.1.2	0.6	5	1	6	0.07	0.2		
4.1.3	0.7	5	1	6	0.07	0.2		
4.1.4	1	5	1	6	0.07	0.2		
4.2.1	1	5	1	6	0.07	0.2	B_4	Expt 4.2 /Expt 5.2*
4.2.2	1	6	1	6	0.07	0.2		
4.2.3	1	8	1	6	0.07	0.2		
4.2.4	1	10	1	6	0.07	0.2		
4.3.1	1	5	1	6	0.07	0.2	σ_{100}	Expt 4.3 /Expt 5.3*
4.3.2	1	5	1.5	6	0.07	0.2		
4.3.3	1	5	2	6	0.07	0.2		
4.3.4	1	5	2.5	6	0.07	0.2		
4.4.1	1	5	1	5	0.07	0.2	z_f	Expt 4.4 /Expt 5.4*
4.4.2	1	5	1	6	0.07	0.2		
4.4.3	1	5	1	7	0.07	0.2		
4.4.4	1	5	1	8	0.07	0.2		
4.5.1	1	5	1	6	0.07	0.2	η	Expt 4.5 /Expt 5.5*
4.5.2	1	5	1	6	0.075	0.2		
4.5.3	1	5	1	6	0.08	0.2		
4.5.4	1	5	1	6	0.09	0.2		
4.6.1	1	5	1	6	0.07	0.0	j_0	Expt 4.6 /Expt 5.6*
4.6.2	1	5	1	6	0.07	0.2		
4.6.3	1	5	1	6	0.07	0.3		
4.6.4	1	5	1	6	0.07	0.4		

Table 5. Sets of the Parameters Used for the runs with $\{k = 1, \gamma = 1.1\}$ for the experiments given in Table 3.

Note: For each experiment we specify the parameter sets used. An asterisk indicates that, in addition to the parameter set for Expt 4, we have one more parameter $q = 0.1$ for Expt 5, which prescribes the complete model.

3.1. Summary of Experiments 1-4

Experiment 1 (only accretion) has been discussed in Appendix E, experiment 2 (accretion and stellar capture in full loss cone theory) in Appendix F, experiment 3 (only accretion and BZ effect) in Appendix G and experiment 4 (accretion, stellar capture in steady loss cone and BZ effect; see Table 3) in Appendix H along with their results. Here we present a summary and salient points of these experiments:

1. *Experiment 1* (Appendix E): In experiment 1, we recover the well-known result of Bardeen (1970), where we see that, in the presence of only accretion, the black hole spin saturates very fast, and subsequently only the mass increases, leaving the spin parameter unchanged at the

saturated value of 1. This demonstrates that the effects of mergers and BZ are important components required to spin down the black hole.

2. *Experiment 2* (Appendix F): In experiment 2, we model the mass evolution of the black hole in the presence of accretion (and feedback) and stellar capture in the full loss cone limit. The main usefulness of this result is that we can derive a completely analytic solution in this case, to obtain fiducial timescales, which can be compared with other nearby models. This is a nonrelativistic treatment (sans spin), and it is useful to obtain the time (or redshift) of mass saturation given by Equation (57). Taking into account the saturation, we present the results for the more realistic evolution experiments (3 & 4 in Table 3), where we include the effects one at a time.
3. *Experiment 3* (Appendix G): In experiment 3, we model the mass and spin evolution of the black hole in the presence of accretion and the BZ effect (Mangalam 2015). It can be seen that the BZ torque causes the spin-down of the black hole, reducing it from the highest saturated spin value. As the B_4 value is increased, the spin-down is more effective, while the accretion is enhanced. Also, it can be seen that mass growth by accretion with an efficiency of $\eta = 0.01$ or 0.05 is very small, which cannot generate high-mass black holes in the universe. Therefore, $\eta \geq 0.05$.
4. *Experiment 4* (Appendix H): In experiment 4, we consider the mass and spin evolution of black holes in the presence of accretion, stellar capture, the steady loss cone regime, and the BZ process. The chosen input parameters are given in Table 5. It is seen that BZ moderates the spin evolution. It is seen that spin buildup is not as rapid, but the mass accretion proceeds to saturation similar to experiment 3.

We have discussed how the complete model differs from experiment 4 in §3.2.

3.2. Complete Model with Accretion, Stellar Capture, Mergers, and BZ Torque

Here we add the contribution of mergers to the spin and mass evolution and retain all the terms in Equations (64) and (62) for our calculations (see Figure 9).

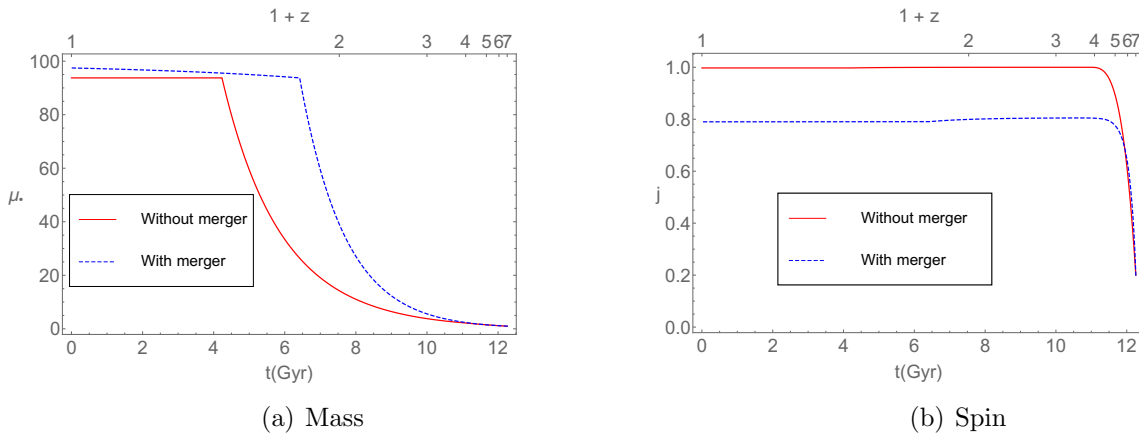


Figure 9. Evolution of $\mu_{\bullet}(t)$ (a) and (b) $j(t)$ of the black hole are shown for the canonical case of the complete model with mergers (run # 5.5.4) and without the effect of mergers with the other parameters being the same.

Our results are the following:

1. We see a change in the slope of the mass evolution in Figure 9(a). This is due to the saturation of black hole mass, where the dominant term, accretion, stops contributing and stellar capture and mergers take over. Since the mass growth rate by accretion is more than the latter two, the slope changes dramatically.
2. From Figure 9 (run # 5.5.4 / 4.5.4) we observe a difference in evolution in the presence and absence of mergers. It is clearly seen that in the presence of the mergers the black hole reaches the saturation mass earlier owing to the higher mass growth rate and that the final mass attained is higher because of the contribution of mergers.
3. As we consider the merger activity to be effective from $z \lesssim 4$, we see that the two curves start deviating from each other after $z \gtrsim 4$ owing to an overall increase in the mass growth rate.
4. We observe from the spin evolution (see Figure 9(b)), that the saturated or the final spins are different for the two cases. This is due to minor mergers that cause the spin-down of the black holes; again, the evolution changes after $z \simeq 4$. This emphasizes the importance of the contribution of mergers and the BZ effect in the spin evolution; otherwise, the black holes will be maximally spinning.

Next, we discuss the evolution in the presence of all the effects and its dependence on the input parameters. Figure 9 represents the evolution for the canonical case (run # 5.5.4). For the runs (run # 5.1 to # 5.6 in Table 5), we discuss our results obtained in Figure 10 for the mass evolution and in Figure 11 for the spin evolution.

1. We found that the mass evolution has a small dependence on the parameters $\{k, \gamma, j_0, B_4\}$ in the input range.
2. If the σ is the same, then the final mass will be almost the same, irrespective of their initial masses [see Figure 10(a)].
3. Change in z_f (run # 5.4) has little impact on the evolution and does not affect the final mass much [see Figure 10(c)].
4. Variation of σ (run # 5.3) shifts the saturation point owing to the dependence on σ [see Equation (57)]. Higher σ implies higher saturation mass and larger time taken to reach the saturation point [see Figure 10(b)].
5. Increase of η (run # 5.5) increases the accretion rate, which is the main source of mass growth. Hence, for higher η , the system reaches the saturation point earlier [see Figure 10(d)].
6. The difference between the complete model (see Figure 10) and Expt 4 (see Figure 26) is that the mass evolution is faster after saturation because of the presence of the merger term, as this contributes along with the stellar capture when the gas accretion stops.

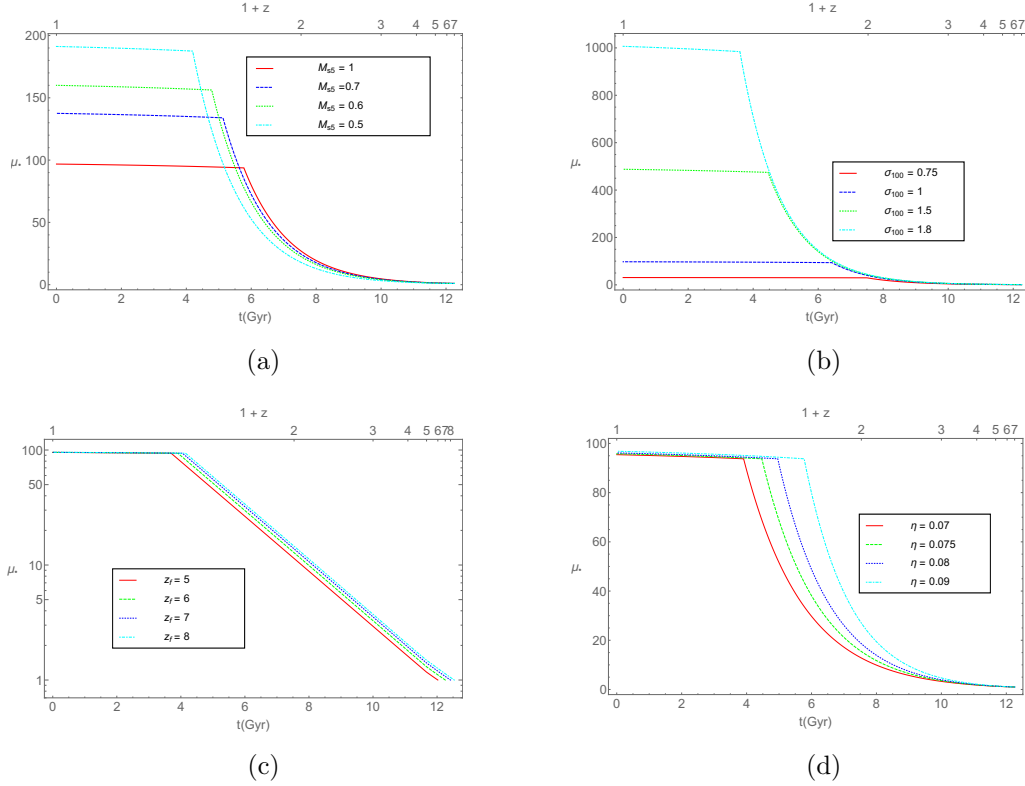


Figure 10. The mass evolution, $\mu_{\bullet}(t)$, for run # 5.1, # 5.3, # 5.4, # 5.5 [see Table 5] (a – d) are shown, when there is accretion, stellar capture, merger and BZ torque present for deviation of various parameters from their values in the canonical set.

7. Again, we observe from run # 5.1 to # 5.6 (see Figure 11) that there is little variation of j for changes in parameters $\{k, \gamma, M_s\}$.
8. Figures 11(a), 11(d), 11(e), and 11(f) show variation at the starting points due to different initial values, but the final values are nearly the same. Therefore, M_s , z_f , η , and j_0 do not affect the final spin value of the black hole.
9. The decrease in j occurs at the high-mass end because of the BZ effect. It is also seen that an increase in B_4 value (run # 5.2) decreases the final spin, as expected.
10. A higher σ (run # 5.3) causes a higher final mass of the black hole; hence, the final spin value decreases with an increase in σ (see Figure 11(c)), while keeping M_s constant.
11. The difference of the complete model with the experiments (3 and 4) is due to the presence of the mergers; the final value of spin acquired is lesser since the minor merger contributes to spinning down the hole (see Figure 11).

Our evolution model is summarized schematically in a flowchart (Figure 8). The motivation is to isolate the contribution of different effects to the evolution of the black hole individually, and also together from $z = z_f \rightarrow 0$. This, in turn, can give us information about for the coevolution of the black hole and the galaxy.

We discuss two applications of the evolution model: the impact on the $M_\bullet - \sigma$ relation and black hole archaeology.

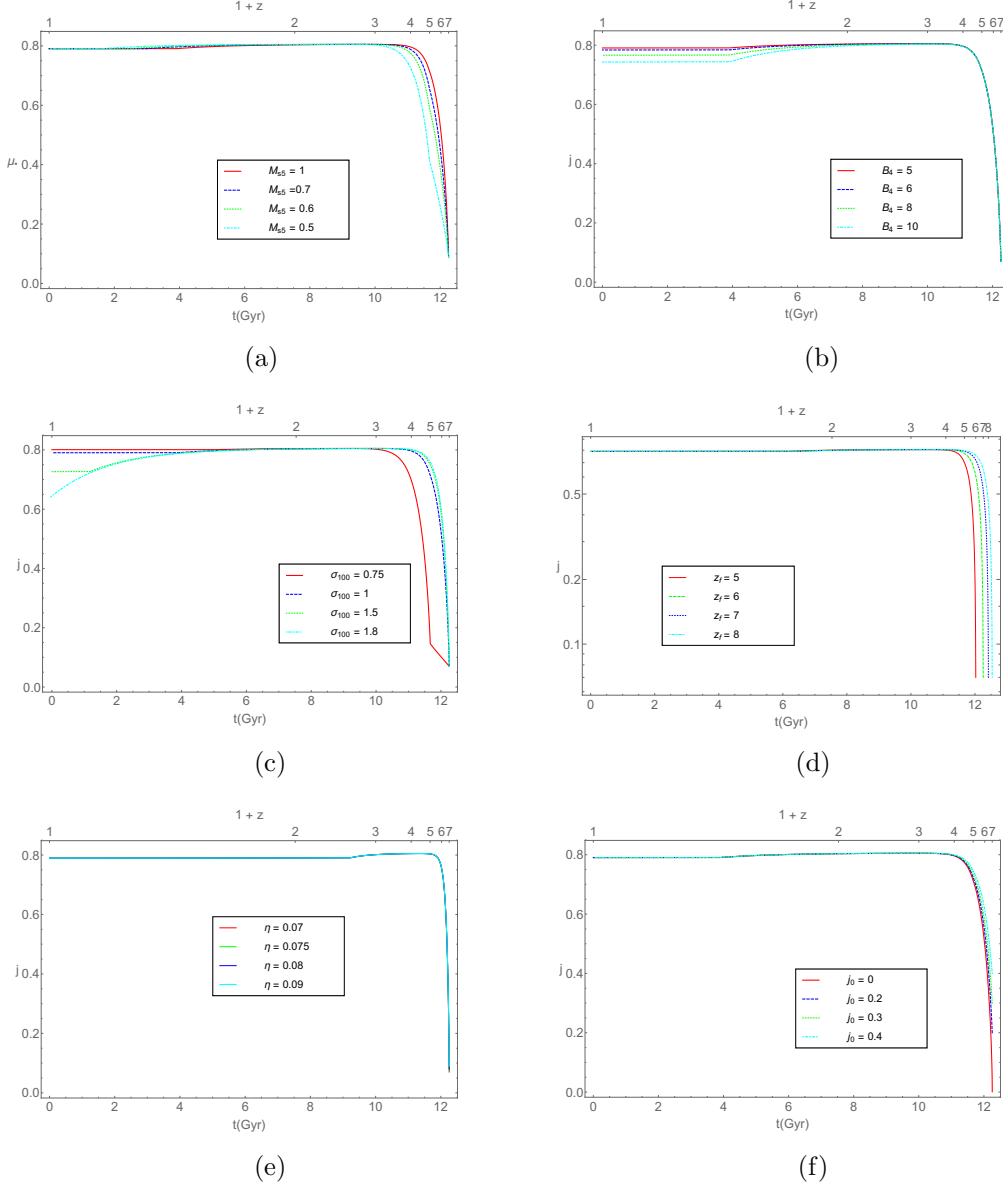


Figure 11. The spin evolution, $j(t)$, for run # 5.1 – # 5.6 [see Table 5] (a – f) are shown, when there is accretion, stellar capture, merger and BZ torque present for deviation of various parameters from their values in the canonical set.

4. APPLICATIONS OF OUR MODEL

4.1. Impact on the $M_\bullet - \sigma$ relation

All the solutions of M_\bullet are dependent on the value of σ , which fixes the value of t_s and z_s for different galaxies given the same M_s . By calculating $M_\bullet(\sigma, z)$, we obtain the evolution of the $M_\bullet - \sigma$ relation. We have assumed that the value σ is constant from formation redshift until the present time since its variation is relatively small and reduces over Hubble time by a factor of $\sim 15\%$ [see

Shankar et al. (2009a), Figure 8]. We have discussed this in §6. In our future models, we plan to include the time variation of σ using an empirical form motivated by Shankar et al. (2009a), which assumes a small variation $\sigma(z) = \sigma_0(1+z)^{-\gamma}$, where σ_0 is the present-day value of σ . But for now, the focus is to isolate all the other effects first. We have calculated $M_\bullet(\sigma, z)$ and derived $p(z)$, the index of the M_\bullet - σ relation [see Fig 12]. In deriving $p(z)$, we have considered the observed range of $\sigma(z)$, to derive the corresponding range of $M_\bullet(z)$ using our evolution model. To start with, we assumed that, at the formation redshift, $p = 5$, which is set by the Faber–Jackson relation. It is a reasonable assumption, given that black hole formation models produce masses proportional to the bulge mass (Mangalam 2001). Even if this were not true for the small initial seed mass, the power-law index $p(z)$ would eventually be dominated by the gas and star accretion that inflates the final mass by a factor $M_\bullet/M_s \simeq 10^3 - 10^4$. This is an initial fiducial value to derive the evolution that clearly does not change the long-term or near-term value of p . At the saturation time, the value of $p = 4$, as predicted by the King (2003) model. Thereafter, the black holes grow by stellar capture and mergers alone. Since the growth rate reduces, the slope almost remains near 4 after the saturation.

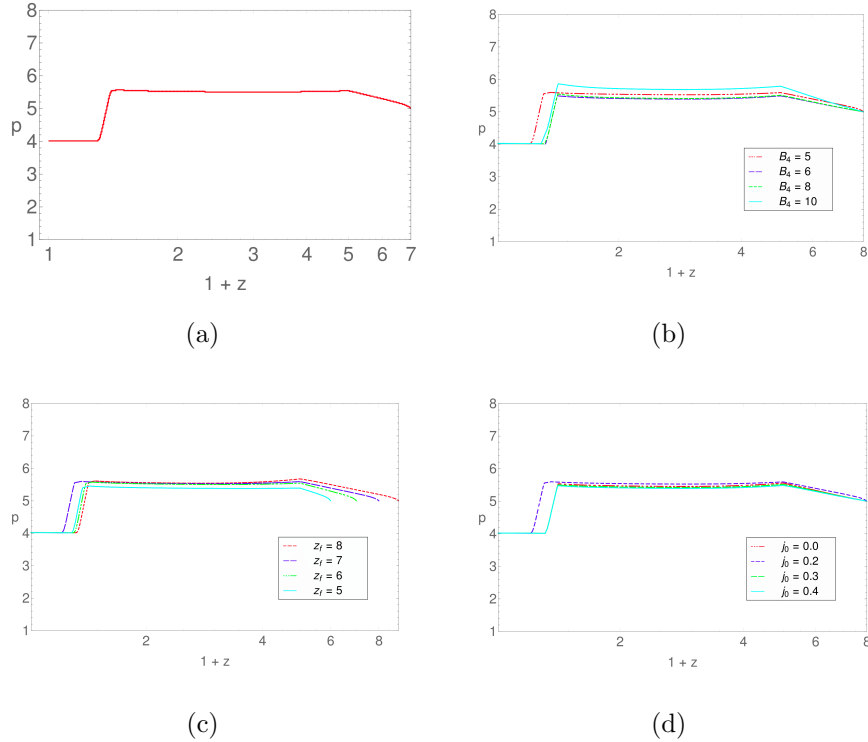


Figure 12. The evolution of $p(z)$ for $\gamma = 1.1$, $M_s = 10^4 M_\odot$ is presented above [Figure 12(a) shows the canonical case, the variation with B_4 is seen in Figure 12(b) for $\{z_f = 7, j_0 = 0.2\}$, the variation with z_f in Figure 12(c) for $\{B_4 = 5, j_0 = 0.2\}$, and the variation with j_0 in Figure 12(d) with $\{z_f = 7, B_4 = 5\}$].

Now, we discuss the dependence of $p(z)$ on the parameters $\{B_4, z_f, j_0\}$. Figure 12(a) in the upper panel of Figure 12 shows $p(z)$ for the canonical case, and Figures 12(b)–(d) show its deviation in the parameter space of $\{B_4, z_f, j_0\}$. We see a change of slope to $p = 4$ near the saturation point as expected, following the dependence for momentum-driven flow [see Equation (57)]. Before z_s , the p value is almost constant, which agrees with the previous work that finds little evolution of the

M_{\bullet} - σ relation. A more accurate evolution can be carried out by considering the mass and redshift distribution function of the black holes to carry out a population synthesis to derive $p(z)$ (Sijacki et al. 2015). In Figure 12, we observe for all the cases that there is a little variation with changes in $\{B_4, z_f, j_0\}$ in the considered range. Thus, we conclude that this relation is expected to be within the observed range of 4–5 as $z_f \rightarrow 0$. Next, we compare our results with data obtained in Bhattacharyya & Mangalam (2018) from the observed intensity profiles of these galaxies listed in Wang & Merritt (2004). These galaxies are within the redshift range 0.004 – 0.002 (see Table 6).

#	Galaxy	M_{\bullet} (in $10^7 M_{\odot}$)	σ (km s $^{-1}$)	z
1	NGC 3379	13.6	230	0.00304 ± 0.00001
2	NGC 3377	2.60	217	0.00222 ± 0.00001
3	NGC 4486	188	433	0.00428 ± 0.00002
4	NGC 4551	3.77	218	0.00392 ± 0.00002
5	NGC 4472	117	542	0.00327 ± 0.00002
6	NGC 3115	17.0	230	0.00221 ± 0.00001
7	NGC 4467	0.493	77	0.00475 ± 0.00004
8	NGC 4365	67.7	453	0.00415 ± 0.00002
9	NGC 4636	58.0	251	0.00313 ± 0.00001
10	NGC 4889	299	467	0.02167 ± 0.00004
11	NGC 4464	1.12	112	0.00415 ± 0.00001
12	NGC 4697	20.76	215	0.00414 ± 0.00001

Table 6. Data from BM18 [Based on Wang & Merritt (2004)] for 12 galaxies Used for matching Our results with observations are given above.

#	References	p	k_0
1	Ferrarese & Merritt (2000)	4.8	0.5
2	Gebhardt et al. (2000)	3.75	0.9
3	Merritt & Ferrarese (2001)	4.72	0.5
4	Ferrarese (2002)	4.58	0.7
5	Tremaine et al. (2002)	4.02	0.83
6	Ferrarese & Ford (2005)	4.86	0.57
7	Gültekin et al. (2009)	4.24	0.7
8	Kormendy & Ho (2013)	4.38	1.48
9	McConnell & Ma (2013)	5.64	0.42
10	Debattista et al. (2013)	4.06	0.97
11	Batiste et al. (2017)	4.76	1.69
12	Sahu et al. (2019)	6.10	0.27

Table 7. Survey of the $M_{\bullet} - \sigma$ relation [see Equation (1)] Giving the Historical Determinations of the Slopes and Constant When M_{\bullet} Is in units of $10^7 M_{\odot}$ and σ is in units of 100 km s^{-1} .

In Figure 13(a), the red curve corresponds to $z = 0.003$ and the green curve corresponds to $z = 0.23$. We see that the red curve gives the better fit to the data presented in Table 6, which is similar to observed values, as the range of redshifts of these galaxies are in the range of 0.001 – 0.004. We

provide a scatter plot of $\{p, k_0\}$ pairs (see Equation (1)) from the literature (shown in Table 7 and Figure 13(b)) below, along with the values obtained from our model, which is within the observed range. The value of p , in our model is nearly 4 owing to the saturation mass used in our evolution model [see Equation (57)], based on the prescription of the momentum-driven flow (King 2003). If the energy-driven flow (Silk & Rees 1998) dominates, we expect $p \simeq 5$ in the local universe. The King (2003) model invokes the presence of cooling sources, whereas the energy-driven flow assumes that there are no cooling processes involved in the medium. Similarly for full loss theory, $\dot{N}_f \propto \sigma^5$. With one or more of the effects of substantial merger rates, full loss cone stellar capture rates, absence of cooling sources, and heavy seeds, the values of $\{p, k_0\}$ can deviate from $\{4, 1\}$ [see Equation (2) in our paper, which represents our basic paradigm]. We hold that the assumptions of the momentum-driven flow and the steady loss cone theory are more appropriate.

Shankar et al. (2009a) analyzed the data of over 40,000 early-type galaxies from the Sloan Digital Sky Survey (SDSS) and they determined $k_0(z) \propto (1+z)^{0.33}$ [see Equation (1)]. According to their analysis, this relation almost holds throughout the age of the universe. Our model also predicts an almost constant p throughout the entire redshift range as expected from Equation (2). We have also shown $k_0(z)$ starting from an approximate value (considering the Faber–Jackson relation with the seed mass within the considered range and σ). Since we have considered a constant σ , $k_0(z)$ is predicted to decrease. According to Shankar et al. (2009a), the M_\bullet – σ relation is given by

$$\log[M_\bullet/M_\odot] = 8.21 + 3.83 \log[\sigma_{200}] + \alpha \log[1+z]. \quad (71)$$

If we consider the relation above using $\alpha = 0.33$ and assume the empirical relation $\sigma(z) = \sigma_0(1+z)^{-0.25}$, where σ_0 is the present-day velocity dispersion to calculate $M_\bullet(t)$, we find that the final M_\bullet is similar to the prediction from our evolution model; see Figure 14(b), which compares $M_{\bullet 5}(t)$ from Equation (71) with our model prediction for ($M_s = 10^5 M_\odot$, $\sigma_{100} = 1$). We see that if the σ stays constant, the final mass attained is also nearly same, which was also concluded by Alexander & Bar-Or (2017).

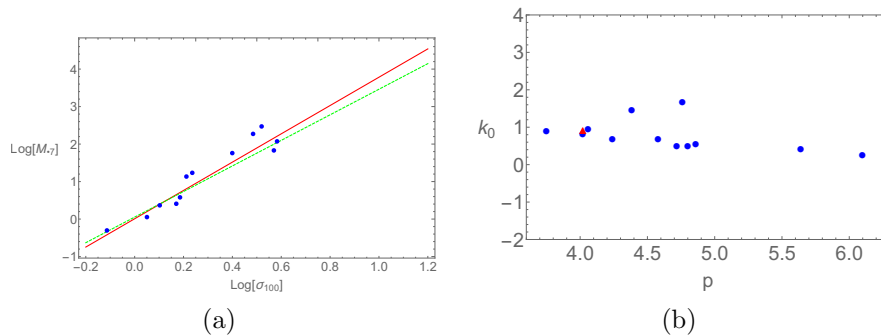


Figure 13. (a) A plot of $\log(M_{\bullet 7})$ vs $\log(\sigma_{100})$ for two different redshifts [$z = 0.003$, (red) and $z = 0.23$, (green)] calculated from our evolution model is shown and compared with the data obtained from our model in BM18 for the 12 elliptical galaxies (whose redshift lies in the range 0.004 – 0.002) and (b) scatter plot of the values of k_0 and p [see Equation (1)] available in the literature (represented by the blue dots) and the red point shows the values obtained using our model.

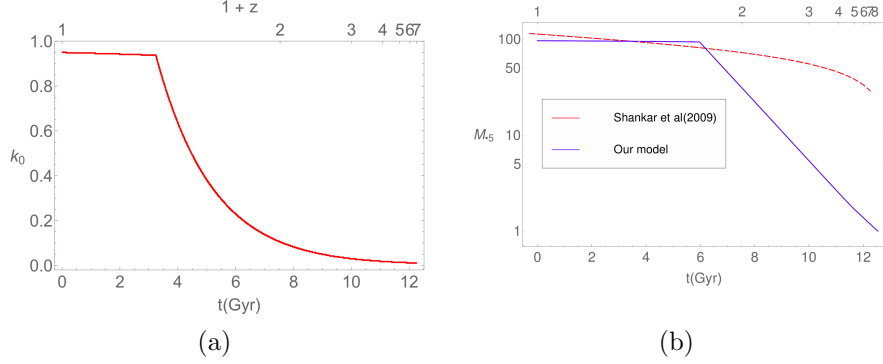


Figure 14. The evolution of the index $k_0(z)$ for $\gamma = 1.1$ is shown for the canonical case (a) and (b) $M_{\bullet,5}(t)$ from prescription of Shankar et al. (2009a) and our model for $M_s = 10^5 M_{\odot}$.

4.2. Black hole archaeology

If we use the final mass and spin as boundary conditions of the mass evolution, we can evolve our model backward in time, a process that we call *black hole archaeology*. Campitiello et al. (2019) analyzed the Optical–UV emission of distant quasars ULASJ134208.10+092838.61 ($z = 7.54$), ULASJ112001.48+064124.3 ($z = 7.08$) and DELSJ003836.10-152723.6 ($z = 7.02$) to study their properties and found the presence of an accretion disk. They used the relativistic disk models KERRBB and SLIMBH to model the emission with approximations to describe the emission as a function of M_{\bullet} , η , j and the viewing angle θ_{ν} . They found that the accretion rate for all sources is sub-Eddington and thus conclude that all three have reached the last stages of their evolution.

#	Input Parameters		Combinations of $\{M_{\bullet,s} \text{ (in } 10^9 M_{\odot}), j_0\}$		
	η	j_f	$z = 10$	$z = 15$	$z = 20$
1	1	0.7	{0.12, 0.76}	{0.06, 0.8}	{0.02, 0.5}
2	0.1	0.7	{0.75, 0.65}	{0.63, 0.55}	{0.6, 0.27}
3	1	0.45	{0.1, 0.7}	{0.05, 0.75}	{0.02, 0.5}
4	0.1	0.45	{0.75, 0.45}	{0.63, 0.38}	{0.6, 0.25}

Table 8. Combinations of Seed Mass and Spin, $\{M_{\bullet,s}, j_0\}$, at $z_f = \{10, 15, 20\}$ for Quasars with Mass $\simeq 10^9 M_{\odot}$ at $z \simeq 7$ for Different Sets of Input Parameters, $\{\eta, j_f\}$, Where, j_f Is the final spin at $z = 7$.

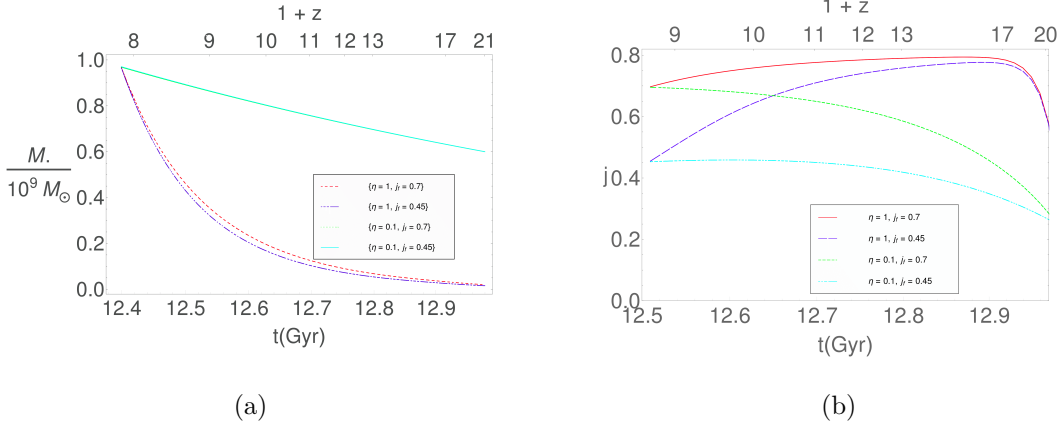


Figure 15. (a) $M_*(t)$ and (b) $j(t)$ evolution for different combinations of η and final spin at $z \simeq 7$, j_f for $z_f = 20$ are shown for final mass at $z \simeq 7$, $M_f \simeq 10^9 M_\odot$.

We observe from the mass and spin values for the quasars listed in Table 1 of [Campitiello et al. \(2019\)](#), (as determined through KERRBB and SLIMBH models), that the following input sets of $\{\eta, j_f\} = \{\{1, 0.7\}, \{0.1, 0.7\}, \{1, 0.45\}, \{0.1, 0.45\}\}$ are suggested. They have also calculated M_* for $j_f = \{0, 1\}$, the extreme ends of the spin values. We have taken the final mass to be $M_* \simeq 10^9 M_\odot$ at $z \simeq 7$ (as suggested by their models) and evolved our model backward for the different sets of $\{\eta, j_f\}$ given above to find the initial seed masses at $z_f = \{10, 15, 20\}$. We see that when $\eta = 1$, the seed mass is also quite small as compared to the case of $\eta = 0.1$ (see Table 8); this is expected owing to the difference in accretion rate [see Figure 15(a)]. The j_f values do not make much difference to $M_*(t)$ when η is fixed. For the case of spin evolution, when $\eta = 1$, j increases and then decreases, but for $\eta = 0.1$, it continues to decrease [see Figure 15(b)]. This is because, for high accretion rate, the spin reaches its maximum value rapidly and then it reduces owing to BZ torque and minor mergers to j_f ; however, when $\eta = 0.1$, the mass growth is slower, so it does not reach the maximum spin within a gigayear, as both BZ and merger terms are mass dependent and hence not as effective. It seems that a heavy seed of nearly $M_s = 10^7 M_\odot$ is required at $z = 20$ even if $\eta = 1$ (see Table 8). This poses difficulties for black hole formation models [eg. [Pandey & Mangalam \(2018\)](#)] or for the mass suggested by [Campitiello et al. \(2019\)](#). One possible resolution can be a two-phase accretion for the growth of quasars, with a short super-Eddington phase in the beginning without considering feedback, under very favorable conditions, in an environment where there is a lot of cold gas around the black hole, followed by a long sub-Eddington phase with feedback effects, as suggested by [Li \(2012\)](#). The existence of a short super-Eddington phase is also suggested by [Campitiello et al. \(2019\)](#) and [Lapi et al. \(2014\)](#). [Campitiello et al. \(2019\)](#) find that if the seed black holes in these sources, with masses in the range 10^2 – $10^4 M_\odot$, grow during $z_f = 20$ – 10 at 15–30 times of the Eddington accretion rate with a low radiative efficiency ($\sim 10\%$), then they can reach the present-day mass within 0.7 Gyr.

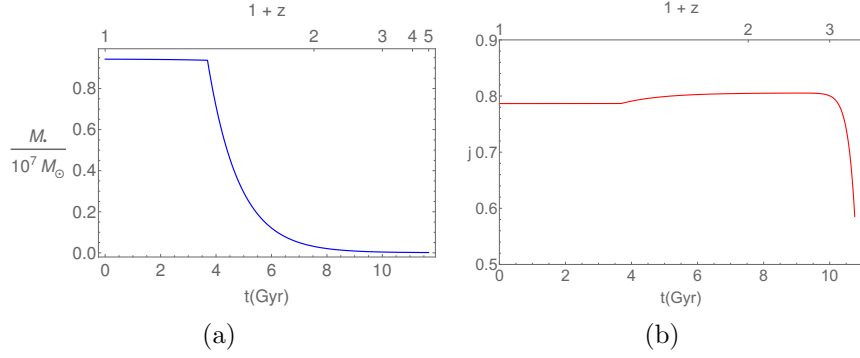


Figure 16. (a) $M_{\bullet}(t)$ and (b) $j(t)$ evolution for the complete model, are shown, starting from final mass $\mu_{\bullet 5} = 94.3$ with other parameters the same as that of run # 5.1.4.

For comparison, we also evolve the final configuration for SMBHs, $\{M_{\bullet} = 10^7 M_{\odot}, j_f = 0.8, z_f = 0\}$, which is shown in Figure 16. We see from Fig 16(a) that the mass reaches a seed value of $3.5 \times 10^4 M_{\odot}$, which is typical, and Figure 16(b) indicates a seed spin of $j_s = 0.58$. With these illustrations, it is clear that our model is a useful tool for black hole archaeology.

4.3. Summary of the Results and Caveats

We summarize our results here.

The key novel aspects of the paper are the relativistic inputs of the capture radius and tidal radius to the loss cone formalism, determining the applicable range of steady loss cone theory, and including all known contributions of gas, stellar, electromagnetic torque, and mergers through detailed formulae as recipes for calculating the joint spin and mass evolution relativistically while taking into account the effects of saturation, merger regimes, and the mode of stellar ingestion. We have applied this elaborate model to make predictions for the capture rate of stars, \dot{N}_s , for the evolution of the $M_{\bullet} - \sigma$ relation and in retrodicting the initial black hole configurations from their more recent inferred ones. The detailed findings are summarized as follows:

1. We calculate r_t using the effective Kerr potential to include the effect of the spin parameter and find $x_t(M_8, j, k, Q)$ (see Figure 18 for both prograde and retrograde cases). We see from Figure 18, that a higher j reduces x_t owing to the relativistic potential. We see that $x_t(M_8, j, k, Q)$ is important in deriving r_t and $l_{\ell}(M_8, j, k, Q)$, which has an impact on \dot{N} . Even a small change in $x_t(M_8, j, k, Q)$ has an impact on $l_{\ell}(M_8, j, k, Q)$.
2. We calculate the loss cone radius $x_{\ell} = \text{Max}[x_t, x_c]$ (Figure 3). For higher-mass black holes, the prograde capture radius x_c goes down dramatically, so it reduces the capture rate. x_{ℓ} (see Figure 3) has an impact on $\dot{N}_s(M_{\bullet}, j, k, Q, \epsilon_s, \sigma)$ which reduces with mass but increases with spin for both the prograde and the retrograde cases. This can be further explored with axisymmetric distributions $f(E, L_z)$, as it is known that the Carter's constant is a function of $L^2 - L_z^2$. A critical mass value of $M_c(j, Q) \simeq 3 \times 10^8 M_{\odot}$ is found; for higher masses r_{ℓ} is set by r_c instead of the tidal radius (the black lines in Figure 2a and Figure 2b show the critical point, when $r_t/r_c = 1$); $M_c(j, Q)$ changes significantly with spin, and this has implications for cosmic evolution and its impact on \dot{N} and black hole growth that need to be further explored (see Figure 2).

3. We also calculate a relativistic correction to the tidal radius given by Equation (21).
4. We calculate the effects of stellar capture for both full and steady loss cone theory. For most cases, we find that the steady loss cone model is appropriate. We have calculated the \dot{N}_s using the prescription given by MM15 (but by not assuming an M_\bullet - σ relation) while adding the relativistic corrections to r_ℓ (as shown in Figure 5) to obtain $\dot{N}_s(M_\bullet, j, k, Q, \epsilon_s, \sigma)$. This is smaller typically by a factor of 10 than the nonrelativistic model of MM15. Our predicted capture rates (see Figure 5) of 10^{-5} to 10^{-6} yr^{-1} can explain the observed rates (Donley et al. 2002; Gezari et al. 2009; Komossa 2015) of around 10^{-5} yr^{-1} (dominated by black holes of $M_8 \lesssim 0.01$) and are a key result.
5. We calculate the impact of the evolution on the spin and mass of the SMBH [Figures 11, 10], and M_\bullet - σ relation (Figure 12) as a function of redshift in a Λ CDM cosmology. We performed five experiments by adding the contributions of gas accretion, stellar capture, BZ effect, and mergers one by one and studied how it impacts the evolution. These are useful illustrations of the individual effects.
6. In Appendix H, we derived the mass evolution in the nonrelativistic case assuming full loss cone theory by analytical expressions considering only accretion and stellar capture. We present the evolution of $M_\bullet(z)$ for different cases in Figure 23. In Appendix G, we have also considered the BZ torque, which contributes to spinning down the black hole with a strong poloidal magnetic field that extracts the spin energy, causing a spin-down of the black hole. Next, we studied the evolution of the spin and mass including all the effects one at a time. Figure 24 shows the evolution in the presence of only accretion and BZ torque, while Figures 27 and 26 show the evolution in the presence of accretion, stellar capture, and BZ torque. All the effects of accretion, stellar capture, mergers, and BZ torque have been included for different parameter sets in Figures 10 and 11. We see that the accretion term dominates over the other terms until saturation. This is because the stellar capture rate decreases with mass, and at the same time the mass growth rate by accretion increases. The mergers and stellar capture contribute significantly to the mass growth after the halt of accretion. The merger activity drops off after $z \gtrsim 4$. Therefore, in the presence of the merger term, the mass and spin evolution start to deviate from those of the case for evolution without mergers near $z \simeq 4$; due to an overall increase in the mass growth rate, the saturation occurs earlier, and the final mass of the black hole is also higher than that of the case for evolution without mergers.
7. We compare our results of $p(z)$ with available observations (see Figure 13(a) and Table 6) given in Bhattacharyya & Mangalam (2018), where σ was calculated from observed intensity profiles for a set of galaxies given in Wang & Merritt (2004).
8. We model $p(z)$ in the range $z = z_f \rightarrow 0$ with a constant σ , assuming that minor mergers do not change it substantially. This is seemingly consistent with observed p in the nearby redshift range. But our predictions need to be tested by simulations and data available from future missions like the Thirty Meter Telescope (TMT), Very Large Telescope (VLT), and Extremely Large Telescope (ELT).

9. We have assumed that the seed mass $M_s \propto \sigma^5$, as suggested by the Faber–Jackson relation for deriving the evolution of the M_\bullet – σ relation, as an application of our evolution model. Subsequently, the black hole grows, impacting $p(z)$.
10. We conclude that $p(z)$ changes gradually with redshift. Therefore, we expect that the late-type galaxies will have a higher p compared to the early-type galaxies as suggested by [McConnell & Ma \(2013\)](#).
11. Our model is useful for carrying out black hole archaeology. Figure 16 shows the evolution obtained when we run our model backward using the present-day initial conditions of $\{M_\bullet, j\}$ and we find that $M_s \simeq 3.5 \times 10^4 M_\odot$, which is within the range of seed masses considered in the literature.

We discuss these results in the next section.

5. DISCUSSION

Stellar capture rate of black holes: The rates of TDEs for a single black hole in steady state have been derived by different authors as already mentioned in §1, with various physical effects included such as the Nuker profiles ([Syer & Ulmer 1999](#)), nonspherical galaxies ([Magorrian & Tremaine 1999](#)), resonant relaxation ([Rauch & Tremaine 1996](#)) and its quenching by relativistic precession ([Rauch & Ingalls 1998](#)), and black hole spin ([Kesden 2012](#)). The theoretical estimates range from 10^{-6} to 10^{-4} yr $^{-1}$ for the most part, while the observational results of [Komossa \(2015\)](#), [Donley et al. \(2002\)](#) (ROSAT surveys), and ([Gezari et al. 2009](#)) (in UV band) have provided rates of TDEs for different wavelength bands to be about $\lesssim 10^{-5}$ yr $^{-1}$. MM15 model the nonrelativistic steady-state loss cone regime, taking into account the angular momentum dependence. We have expanded the theory to include relativistic effects in a Kerr potential to calculate the tidal and capture radius, which in turn, is an input to the loss cone theory that determines the rate of stellar capture. MM15 considered nonrelativistic theory and used $L_\ell(\sigma, r_t) = \sqrt{2r_t^2\phi(r_t) - E}$. In our relativistic model, the loss cone angular momentum $L_\ell(j, k, x_\ell, Q)$ is given by Equation (24), where the loss cone radius x_ℓ is used instead of x_t used in MM15; this causes a decrease in the value of \dot{N}_s by a factor of a few, due to the decrease of the loss cone radius, bringing it more in line with observed estimates.

[Alexander & Bar-Or \(2017\)](#) determined the minimal mass of the present-day black holes by including the stellar capture process. They conclude irrespective of the seed masses that if σ of the galaxies are nearly equal, then all the black holes reach almost the same mass, assuming that the M_\bullet – σ relation holds throughout. All the black holes grow over the age of the universe to the present-day mass scale of $M_6 \gtrsim 0.2$ (with 5% lower confidence level), independent of their initial seed mass and the formation process. They conclude that the present-day M_\bullet is nearly independent of the uncertainties in z_f , and provide a universal minimal mass estimate for the black holes that grow by gas accretion or mergers. This can explain the reason for not finding any intermediate-mass black holes with $M_6 \lesssim 0.2$, which in turn implies that present-day galaxies that have $\sigma \lesssim 35$ km s $^{-1}$ (at 5% lower confidence level) do not contain a central black hole. We derive the evolution without any a priori assumption of M_\bullet – σ relation throughout and also take into account all major effects causing the growth of the black hole including relativistic effects of stellar capture and spin evolution, which were not considered by [Alexander & Bar-Or \(2017\)](#). Our result agrees with their finding that the final mass attained by the hole is nearly independent of the formation time. Figure 6 shows the mass evolution in the presence

of only stellar capture, which matches the result of Alexander & Bar-Or (2017) [see Figure 6]. The black holes with higher seed masses will reach the saturation point earlier, as they will grow lesser by accretion and more by mergers and stellar capture as compared to the lower-mass seed black holes.

The stellar capture process can indeed be important for the formation of the SMBH seeds. Recently, Boco et al. (2020) have suggested that the mergers of stellar mass black holes and neutron stars via gas dynamical friction in $\sim 10^7$ yr and in a dense cluster, whose size is \sim kpc and contains very high gas mass of $\sim 10^{10}M_\odot$ (leading to a high density of $10M_\odot \text{ pc}^{-3}$), form 10^4 – 10^6M_\odot seeds. Our proposal is different: using our relativistic steady loss cone theory (in a not so dense cluster and hence neglecting dynamical friction), the mass growth rate due to stellar capture alone can be approximated from our numerical model [see Figure 5] to be

$$\dot{M}_{\bullet*} = 5 \times 10^{-6} M_6^{-0.33} M_\odot \text{yr}^{-1}, \quad (72)$$

for typical values of $\sigma = 200 \text{ km s}^{-1}$ and $\gamma = 1.1$. The rate of mass growth by accretion process is given by

$$\dot{M}_{\bullet g}(\eta) \simeq 10^{-2} \eta M_6 M_\odot \text{yr}^{-1}. \quad (73)$$

From Equations (72) and (73), we find that the critical mass below which stellar capture dominates over accretion is given by $M_{*c}(\eta) \simeq 5 \times 10^3 \eta^{-0.75} M_\odot$. Therefore, stellar capture can be an important process for forming SMBH seeds with $M_{\bullet s} \lesssim M_{*c}$.

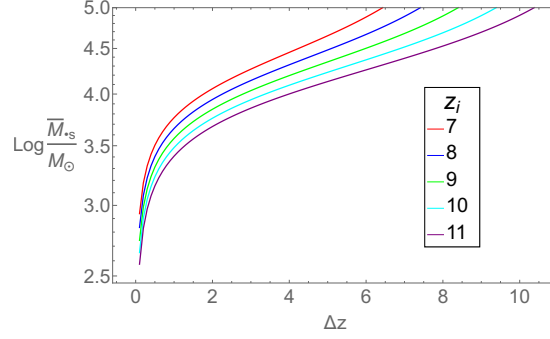


Figure 17. The mass growth as a function of change in redshift is shown above where it is seen that $10^4 M_\odot$ seed is obtained for $\{z_i, z_f\} = \{\{11, 7.01\}, \{10, 6.63\}, \{9, 6.21\}, \{8, 5.74\}, \{7, 5.23\}\}$.

Solving Equation (72), for $\sigma = 200 \text{ km sec}^{-1}$ and $\gamma = 1.1$, we arrive at

$$\Delta \bar{M}_\bullet = \bar{M}_{\bullet s} - \bar{M}_{\bullet*}; \quad \bar{M}_{\bullet s}^{1.33} - \bar{M}_{\bullet*}^{1.33} \simeq \bar{M}_{\bullet s}^{1.33} = 6.35 \times 10^5 \Delta t; \quad \Delta t = t(z_f) - t(z_i); \quad \Delta z = z_i - z_f, \quad (74)$$

where the masses are in units of M_\odot , and $\Delta t = t(z_f) - t(z_i)$ [see Equation (69) for $t(z)$] is in units of Gyr. $\bar{M}_{\bullet s}$ is the seed mass formed at z_f , and $\bar{M}_{\bullet*}$ is the mass of the stellar mass black hole at an initial redshift of z_i . Δt can be expressed as a function of $\Delta z = z_i - z_f$ and z_i using Equation (69) in our paper, so that $\Delta \bar{M}_\bullet(z_i, \Delta z) \simeq \bar{M}_{\bullet s}(z_i, \Delta z)$. From the Figure 17, we see that the seed mass reaches $\sim 10^4 M_\odot$ for the following combinations of initial and final redshifts: $\{z_i, z_f\} = \{\{11, 7.01\}, \{10, 6.63\}, \{9, 6.21\}, \{8, 5.74\}, \{7, 5.23\}\}$. Therefore, stellar capture can be considered as

a viable process for formation of SMBH seeds where it is seen that SMBH seeds of $10^4 M_\odot$ can be formed in 10^7 – 10^8 years depending on the initial redshift range, $z_i = 7$ – 10 . For binary systems, the rate can be higher by an order of magnitude compared to our case, as shown by [Thorp et al. \(2019\)](#), which is comparable to MM15.

Mass and spin evolution of the black hole: The spin and the mass evolution of an SMBH are mainly dependent on three processes: gas accretion, the capture of stars, and mergers. We built a formation for relativistic loss cone theory and included it in the mass and spin evolution of black holes. For accretion, we have used a constant sub-Eddington accretion efficiency throughout the process, taking into account duty cycles. In the case of gas accretion with cooling sources, the flow is momentum driven ([King 2003](#)). The stellar capture rate has been carried out in both full and steady loss cone theory frameworks. We have incorporated the prescription of saturated mass by [King \(2003\)](#), which causes a halt in accretion, leaving the stellar capture and mergers as the only channels to contribute to the growth of the black hole. For the mass growth of SMBHs by mergers, we have considered both the contributions of major and minor mergers ([Stewart et al. 2009](#)). The rate of minor mergers is more frequent compared to the major ones. However, major mergers contribute to spinning up the black hole, while minor mergers spin it down ([Gammie et al. 2004](#)). We neglect the contribution of the major mergers in spinning up the hole and consider only the effect of the minor mergers in spinning down the hole. We have considered the mergers to be effective for $z \lesssim 4$.

We now compare our results with previous studies. [Mangalam \(2015\)](#) used a theoretical model for mass and spin evolution of the accreting black hole taking into account the spin-down torque caused by the electro-dynamical jet. The evolution in the presence and absence of accretion was studied for different cases such as the thin disk, Bondi accretion, and the MHD disk. When accretion stops, the jet power shows an increase before a gradual decrease if the initial spin, $j > \sqrt{3}/2$, because of the increase in the size of the black hole. The results indicate that the black hole achieves the maximum spin value in the absence of a jet. We expanded these evolution equations to include terms representing stellar capture and mergers. [Dubois et al. \(2014\)](#) have derived the mass evolution from simulations caused by accretion and mergers and applied semianalytic methods for spin evolution. Our results agree with their findings that the low-mass black holes grow their mass mainly by the accretion process, whereas high-mass black holes ($> 10^8 M_\odot$) grow their mass mostly by mergers. This is because accretion halts owing to saturation beyond $M_\bullet > M_{\bullet, \text{sat}}$ while the low-mass black holes grow slowly by stellar capture. We have considered a constant rate of Eddington accretion, while they have considered it to be reducing over time owing to gas rarefaction in galaxies. The justification for considering our parameter ranges is given in §3. From [Figure 9](#), we see a change in the slope of mass evolution near the saturation time. This is expected since the accretion of gas stops and stellar capture and merger activity take over for subsequent growth. The rate of growth for mass accretion is much greater than the other two channels, so the halt of accretion causes the slope change. [Zhang & Lu \(2019\)](#) have studied the spin evolution via two-phase accretion and have found that higher-mass black holes have intermediate spin (~ 0.5), while the low-mass black holes have higher spin ($\gtrsim 0.8$). In our paper, we have studied accretion only in the thin-disk mode ([Shen et al. 2008](#); [Schulze & Wisotzki 2010](#); [Suh et al. 2015](#)). The low value of spin for higher masses can be explained as follows: when the BZ effect dominates, it causes the spin-down of the black hole, while it is possible that the low-mass black holes are a result of gas accretion alone and without mergers; hence, the spins are higher. [Zhang & Lu \(2019\)](#) have also used a power-law dependence of the radiative efficiency

with the black hole mass where it decreases with an increase in mass, though they have found the dependence to be weak. This is in contradiction with the model of [Davis & Laor \(2011\)](#), who claim an increase with mass with a power-law index of 0.5. Here, we aim to capture a complete picture of black hole growth using all the factors contributing to it, and for simplicity, we consider the radiative efficiency, ϵ_M , to be constant with respect to mass (but varying as a function of j), with a goal to study and compare all the other contributing factors. We intend to include the mass variation of radiative efficiency in the future. However, the dependence is weak, and it is not likely to make a significant difference to our results. Recently, [Shankar et al. \(2020\)](#) suggested a higher mean radiative efficiency, $\epsilon_M \sim 0.15$, which is defined as $\epsilon_M = L/\dot{M}_0 c^2$, where L is the luminosity and \dot{M}_0 is the rest mass accretion rate. We can write $\epsilon_M(j) = 1 - \epsilon_I(j)$ following the standard prescription of [Bardeen et al. \(1972\)](#), [Shapiro \(2005\)](#), and [Mangalam \(2015\)](#) for the thin-disk case, where $\epsilon_I(j)$ is given by Equation (6) in our paper. This factor $\epsilon_M(j)$ is shown in Figure 7 of [Shankar et al. \(2020\)](#); they conclude from observational values, using their de-biased relation of black hole mass and star mass, that a steady-state value of $\epsilon_M \sim 0.15$ is expected. In our theoretical evolution model, we use the standard relativistic form of $\epsilon_M(j)$ which varies between $(1 - \frac{2\sqrt{2}}{3}) \simeq 0.06$ (for $j = 0$) and $(1 - \frac{1}{\sqrt{3}}) \simeq 0.42$ (for $j = 1$). The mean value is approximately 0.24, which, after incorporating the duty cycle, can reduce further [to values near 0.15 as suggested by [Shankar et al. \(2020\)](#)].

From Figure 9, we see that the spin of the black hole initially increases because of accretion, after which there is a spin-down due to the BZ torque. Since we have considered a thin-disk accretion, the spin value very quickly reaches the maximum spin as mentioned by [Li \(2012\)](#). [Gammie et al. \(2004\)](#) showed how accretion, major mergers, and minor mergers contribute to the spin evolution of the black hole. Using the prescription given by [Gammie et al. \(2004\)](#) for minor mergers, we see that the value of the maximum spin attained is much less than those where the contribution of mergers is included. We have incorporated minor mergers only for spin-down of the hole, as the spin-up process is already dominated by the accretion process.

Our model is useful for retrodicting the initial black hole configuration when we run our model backward from the observed $\{M_\bullet, j\}$ as the initial conditions as shown in §4.2. More observations and models that provide the final $\{M_\bullet, j\}$ state will provide useful clues for such exercises in black hole demographics.

Evolution of the M_\bullet - σ relation: We have combined all the known effects contributing to the mass and spin evolution of the black hole and thus derived the evolution of the $M_\bullet = k_0(z)\sigma^{p(z)}$ relation by semianalytic methods; some preliminary results were shown in [Bhattacharyya & Mangalam \(2018\)](#). [Shen et al. \(2015\)](#) and [Salviander & Shields \(2013\)](#) have studied the evolution of the relation from SDSS data for quasars and have found no evolution of the M_\bullet - σ relation up to $z \simeq 1$. Numerical simulations of the large-scale structure of the universe by [Sijacki et al. \(2015\)](#) and [Taylor & Kobayashi \(2016\)](#) show that this relation holds almost up to $z \simeq 4$. [Robertson et al. \(2006\)](#) have studied the evolution of this relation until $z = 6$ for merging disk galaxies through hydrodynamic simulations while taking into account the effects of accretion and supernovae. They have found almost no change in $p(z)$ and a very small change of $k_0(z)$ similarly as suggested similarly by [Shankar et al. \(2009a\)](#). From their analysis, $k_0(z) \propto (1+z)^\alpha$, with $\alpha = 0.33$. In our analysis, since we consider σ to be a constant throughout, so that the value of k_0 is expected to decrease at higher redshift as seen in Fig 14(a). At the saturation point, the value of $p \simeq 4$ from our model following [King \(2003\)](#). We have

considered a range of values of $\sigma_{100} = \{1 - 2\}$, which is the average observed range of σ for different galaxies, and assumed $M_{\bullet}(z = z_f) \propto \sigma^5$ as set by the Faber–Jackson relation. From Figure 12, we see that $p(z)$ remains in the range of 4 – 5 throughout, which roughly agrees with the empirical result of Shankar et al. (2009a). Figure 12 shows higher values of $p(z)$ at higher redshifts. Therefore, we conclude that $p(z)$ will be higher for late-type galaxies as suggested by McConnell & Ma (2013). One possibility is that the σ varies with redshift owing to major mergers, but this is outside the scope of this paper. For minor mergers, a constant σ is a reasonable assumption that is based on the work of several authors [Bezanson et al. (2009), Oser et al. (2012), Hopkins et al. (2009), and the dissipative model described by Shankar et al. (2009a)], where they have found that σ changes little with redshift [σ reduces over Hubble time by a factor of $\sim 15\%$, Shankar et al. (2009a)]. The elliptical galaxies that obey the M_{\bullet} – σ relation are within this specified redshift. We conclude from our simulations that although $p(z)$ varies with $\{j_0, B_4, z_f\}$, it stays within the predicted range of 4 – 5.

6. CONCLUSIONS

Our model of deriving the joint evolution of black hole mass, spin and M_{\bullet} – σ relation throws light on the coevolution of the black hole and its environment from the time of formation. We have incorporated all the factors contributing to the growth of the black hole to build a comprehensive evolution model of the black hole.

1. We have included relativistic effects in the process of tidal and direct capture. A key consequence is that the capture rate reduces to the range $10^{-5} - 10^{-6} \text{ yr}^{-1}$, which is more in line with observations.
2. We have built a semianalytic self-consistent evolution model of the black hole.
3. We have explored the roles and phases of importance of each of the growth channels. Though the contributions from stellar capture ($\sim 3\%$) and mergers ($\sim 2\%$) in mass growth of the black hole are small compared to accretion ($\sim 95\%$), irrespective of the parameters before saturation, these two factors play a major role after the saturation when the accretion process stops or contributes negligibly (King 2003). The estimates of the contribution of the effects mentioned here are computed for the canonical case, and this can vary up to 5% within the context of our model assumptions and the chosen parameter ranges. The stellar capture contributes to the mass growth while not changing the spin substantially, whereas the mergers contribute to both. Minor mergers reduce the maximum spin value achieved by accretion by $\sim 20\%$. BZ torque does not contribute to mass growth, but only to the spin-down of the black hole (in the presence of all the effects, for $B_4 = 10$, the spin-down is $\sim 3\%$ from the maximum value attained owing to accretion) as discussed in §2.4. Mergers and the BZ process are necessary; otherwise, the black holes will be spinning maximally.
4. We illustrated the effect of saturation on the evolution of the $M_{\bullet}(z) = K_0(z)\sigma^{p(z)}$ relation.
5. By running the models backward in time, we retrodict the formation parameters of seed black holes. This will enable us to discriminate among models of black hole formation.
6. Stellar capture can be considered as a viable process for formation of SMBH seeds, as this dominates the accretion process when $M_{\bullet} \leq 2 \times 10^4 M_{\odot}$.

7. We expect our transparent and detailed formulation in a fully relativistic framework to be useful for future simulational studies.

This model can be improved by incorporating a model for time variation of η which is an uncertain input. The data from future surveys at high redshift, for example, from TMT, VLT, and ELT, along with measurements of σ from SKA, can be used to probe the M_\bullet - σ evolution to test our model. We also plan to work on the demographics of the black hole, based on a model of seed mass and spin distribution functions.

We would like to thank the anonymous referee for the constructive comments that helped us to improve the paper. We acknowledge DST SERB CRG grant No. 2018/003415 for financial support. We would like to thank Saikat Das for helping us with Figure 7. We acknowledge IIA for the use of the HPC facility for computations and Kavalur Observatory (VBO) for hospitality during our visits. We thank P. Natarajan for discussions during our visit to ICTS (supported by ICTS/smbh2019/12).

APPENDIX

A. ANALYTIC APPROXIMATION TO THE TIDAL RADIUS AND NUMERICAL STATISTICS TO THE TIDAL RADIUS

Taking $y = 1/x_t$ and $\tilde{y} = y/y_{t0} = 1 + \delta$, we find the first-order approximation to y defining y_{t0} as the inverse of the dimensionless tidal radius to be

$$y_{t0} = \frac{1}{x_{t0}} = M_8^{-\frac{1}{3}} \left(\frac{\rho_*}{\rho_\odot} \right)^{-\frac{1}{3}} 10^5 \cdot r_g \text{ pc}^{-1}.$$

The sixth-order equation for δ is

$$2(1 + \delta)^3 - 3(l^2 + Q)y_{t0}(1 + \delta)^4 + 12(1 + \delta)^5[(j - l)^2 + Q]y_{t0}^2 + 10j^3Qy_{t0}^3(1 + \delta)^6 - 1 = 0. \quad (\text{A1})$$

Solving Equation (A1) numerically, we obtain $\delta(j, Q)$.

1. $x_t(M_8, j, Q = 0)$ is shown in Figure 18, where we see that at a fixed j , x_t decreases with an increase of M_\bullet . In the high-mass regime, the variation of x_t is small with spin, but it shows more variation in the low-mass regime, which is also reflected in the calculation of the rate of star capture presented later in this §2.
2. We find that for a fixed value of j , x_t has a small dependence on Q as a function of M_8 . However, $x_t(M_8, j, Q)$ decreases as a function of Q for the retrograde case for a fixed value of M_\bullet . But for the prograde case, $x_t(M_8, j, Q)$ initially decreases for higher Q , but subsequently it shows an increase with increasing Q . $x_\ell(M_8, j, k, Q)$ for different Q values, are shown in Figure 19, for both prograde and retrograde cases.

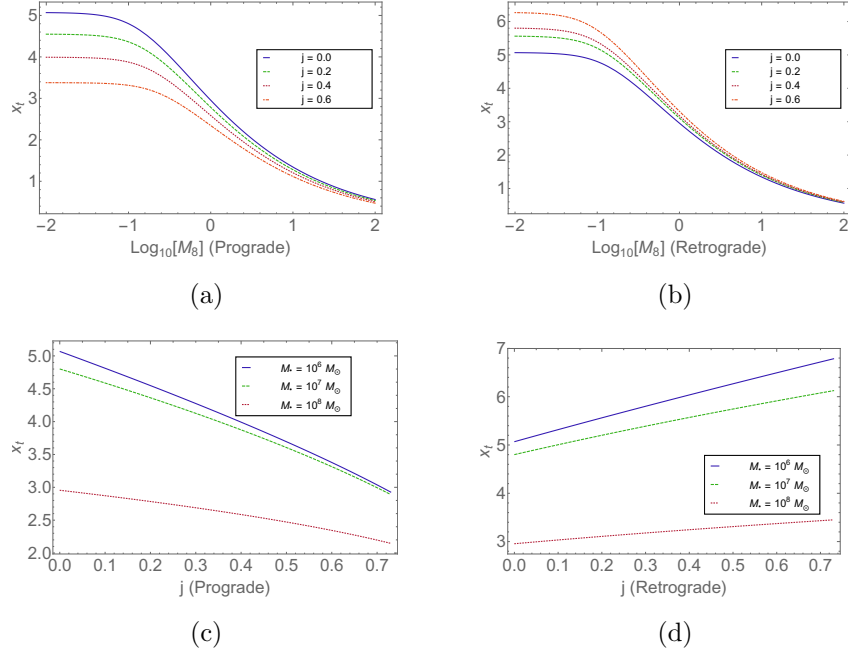


Figure 18. Tidal radius $[x_t(M_8, j, Q) = r_t(M_8, j, Q)/r_g]$ given by Equation (21) is shown as a function of M_8 (panels (a) and (b)) and j (panels (c) and (d)) for $Q = 0$, or prograde (panels (a) and (c)) and retrograde (panels (b) and (d)) motion.

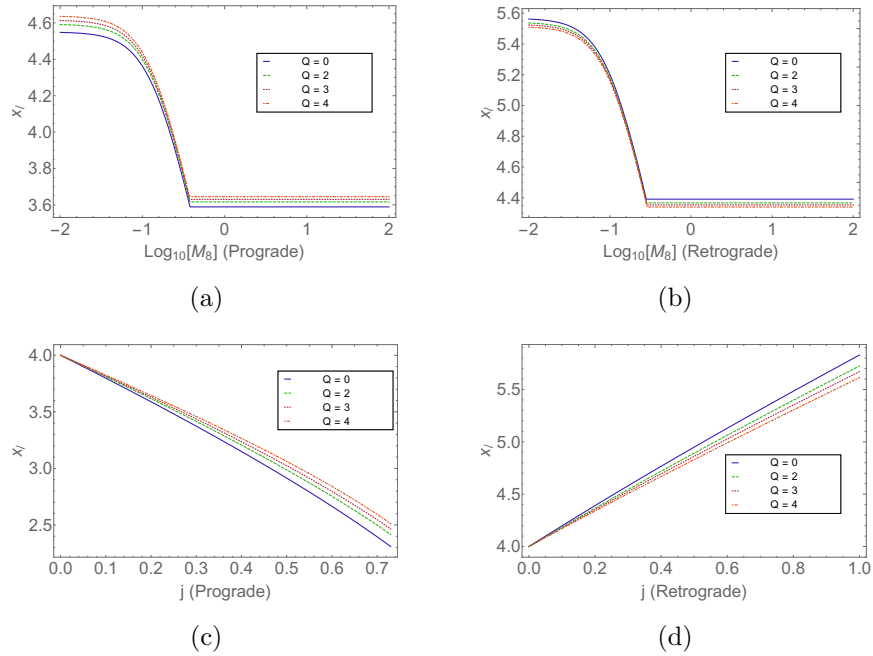


Figure 19. The loss cone radius $[x_l(M_8, j, Q) = r_l(M_8, j, Q)/r_g = \text{Max}[r_t(M_8, j, Q), r_c(M_8, j, Q)]/r_g]$ is shown as a function of M_8 for $j = 0.2$ (a, b) and j for $M_8 = 1$ (c, d) for different Q values, for prograde (a, c) and retrograde (b, d) motion.

B. JUSTIFICATION FOR USING STEADY LOSS CONE THEORY OVER FULL LOSS CONE THEORY

The stars captured populate a loss cone whose angular size is given by (Frank & Rees 1976)

$$\theta_\ell^2(r) = \frac{r_c}{r^2} \frac{GM_\bullet}{\sigma^2}, \quad (\text{B2})$$

where θ_ℓ is the half angle of the loss cone. The angle scattered in a dynamical time $t_d = r/\sigma$ is approximated by

$$\theta_d = \sqrt{\frac{t_d}{t_R}} \quad (\text{B3})$$

$$t_d = \begin{cases} \sqrt{\frac{r^3}{GM_\bullet}} & \text{for } r \leq r_h \\ \frac{r}{\sigma} & \text{for } r \geq r_h \end{cases} \quad (\text{B4})$$

$$t_R = \frac{\sigma^3}{3 \ln \Lambda G^2 m_* n_c}; \quad (\text{B5})$$

where Λ is the Coulomb logarithm of the ratio of maximum and minimum values of the impact parameter and n_c is the cluster mass density, with m_* being the stellar mass (Syer & Ulmer 1999). In the diffusive regime, $\theta_d < \theta_\ell$, the loss cone is empty as the star is removed from the loss cone within a dynamical time scale. At the other extreme, $\theta_d > \theta_\ell$, the loss cone is always full. Both the regimes are shown in Figure 20 for $m_* = M_\odot$ and $n_c = 10^4 M_\odot \text{pc}^{-3}$ for the mass range $M_\bullet = 10^4 - 10^8 M_\odot$ (we have assumed the $M_\bullet - \sigma$ relation with $p = 4$).

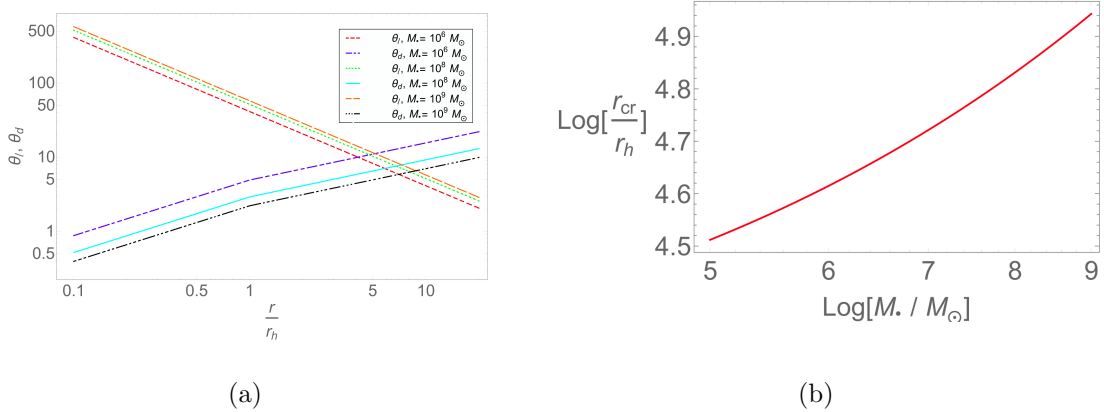


Figure 20. Variation of the angular size of loss cone, θ_ℓ and angle scattered in dynamical time, θ_d with r/r_h for $m_* = M_\odot$ and $n_c = 10^4 M_\odot \text{pc}^{-3}$, for the range $M_\bullet = 10^4 - 10^8 M_\odot$ (a) and (b) the variation of the crossing point, $r_{cr}(M_\bullet)$ defined by $\theta_\ell(r_{cr}) = \theta_d(r_{cr})$, for $m_* = M_\odot$ and $n_c = 10^4 M_\odot \text{pc}^{-3}$ (Syer & Ulmer 1999).

From Figure 20, we see that as the mass of the black hole increases, the crossing point (r_{cr}/r_h) of the two curves shifts toward the right, which implies that the diffusive region expands with an increase in mass.

C. CALCULATION OF THE STELLAR CAPTURE RATE

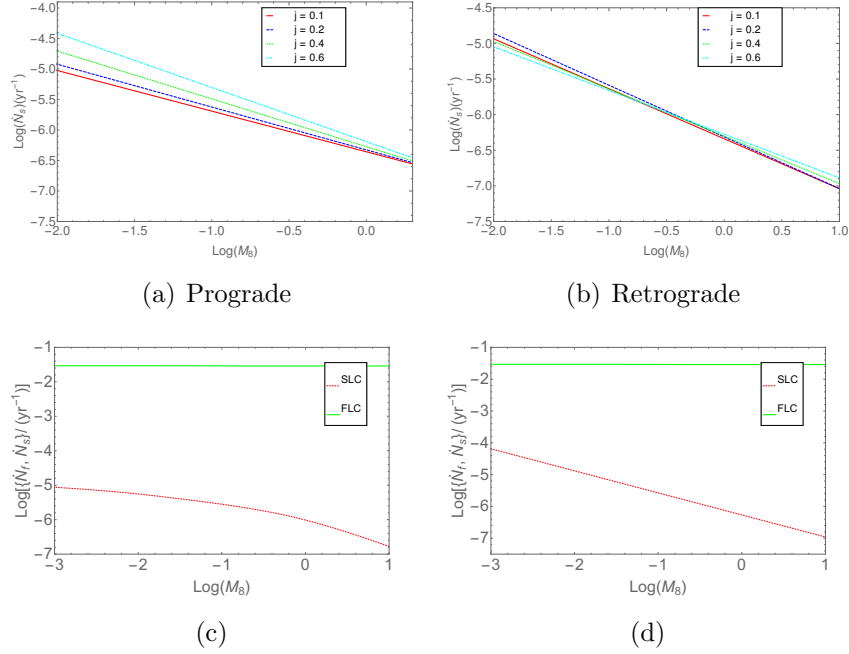


Figure 21. Capture rate, $\dot{N}_s(M_\bullet, j, k, Q, \epsilon_s)$, is shown for different values of j using the M_\bullet - σ relation ($p = 4.86$), where (a) $k = 1$ for the prograde case and (b) -1 for the retrograde case, with the lower limit of ϵ_s taken to be $\epsilon_m = -10$, $\gamma = 1.1$. (c, d) \dot{N}_f and $\dot{N}_s(M_\bullet, j, k, Q, \epsilon_s, \sigma)$ are shown for both the steady and the full loss cone theory with $j = 0$, $Q = 0$, $k = -1$, $\gamma = 1.1$, $\epsilon_m = -10$ and $\sigma = 200 \text{ km s}^{-1}$ using the M_\bullet - σ relation with $p = 4.86$, $\gamma = 1.1$, $k = -1$.

From the bottom panels of Figure 21, we see that the rate of the number of stars falling into the loss cone is higher in the case of full loss cone theory than in the case of steady loss cone by an order of magnitude. Also, the slope is positive at the lower-mass end, and it becomes negative as it reaches the higher mass. \dot{N}_f is almost constant and mainly dependent on the σ term, throughout the whole range, because its dependence on mass through l_ℓ^2 is small, while the mass dependence of \dot{N}_s is strong. We determine the slope of the steady loss cone rate for both the curves with and without using the M_\bullet - σ relation. Without applying the M_\bullet - σ relation, the slope is -0.3 , and by applying the relation with $p = 4.86$, the slope is -0.6 . Therefore, we conclude that \dot{N}_s using the M_\bullet - σ relation is smaller than for the case assuming σ independent of mass.

D. CALCULATION OF TIMESCALES OF SPIN AND MASS EVOLUTION FOR ALL THE EFFECTS

1. *Gas accretion:* From Equation (66) we see that

$$\tau_{M,g} = \frac{M_\bullet}{\dot{M}_{\bullet,g}} = \frac{1}{k_1} \simeq 1 \text{ Gyr}, \quad (\text{D6})$$

and from Equation (E13)

$$\tau_{j,g} = \frac{M_\bullet}{\dot{M}_{\bullet,g}} \left(l_I(j) - 2\epsilon(j)j \right) \simeq 1 \text{ Gyr} \quad (\text{D7})$$

2. *Stellar Capture*: We estimate from Equation (66) that

$$\tau_{M,*} = \frac{M_\bullet}{\dot{M}_{\bullet,*}} = \frac{M_\bullet}{M_\odot} 10^{5.5} \text{ yr} \simeq 10 \text{ Gyr for } M_\bullet = 10^5 M_\odot \quad (\text{D8})$$

3. *Merger*: Also from Equation (47) we find

$$\tau_{M,m} = \frac{M_\bullet}{\dot{M}_{\bullet,m}} = \frac{M_\bullet}{M_5^{1.15} 8.058 \times 10^{-3} \cdot (1+z)^{2.2} 10^5 M_\odot} \text{ Gyr} \simeq 10 \text{ Gyr for } M_\bullet = 10^5 M_\odot, z \simeq 3, \quad (\text{D9})$$

and from Equation (50)

$$\tau_{j,m} = \frac{M_\bullet}{\dot{M}_{\bullet,m}} \left(-\frac{7}{3} + \frac{9q}{\sqrt{2}j^2} \right) \simeq 10 \text{ Gyr} \quad (\text{D10})$$

4. *BZ Torque*: We see from Equation (54)

$$\tau_{j,BZ} = \frac{\mathcal{J}_0}{\mathcal{G}_0} \int_{j_f}^{j_i} \frac{dj}{r^3(j)j} = 7.0 \times 10^8 \text{ yr} \frac{(\kappa(j_i, j_f)/0.1)}{B_4^2 M_9 f_{BZ}} \simeq 1 \text{ Gyr}, \quad (\text{D11})$$

where M_9 is M_\bullet in units of $10^9 M_\odot$ and

$$\kappa(j_i, j_f) = \left[\left(\frac{1}{16} \right) \log \left(\frac{2-w}{w} \right) + \left(\frac{3w^2 + 3w - 4}{24w^3} \right) \right]_{w_f}^{w_i}, \quad (\text{D12})$$

with $w_i = x_+(j_i)$, $w_f = x_+(j_f)$.

E. EXPERIMENT 1: ONLY GAS ACCRETION IS PRESENT

In the presence of only accretion the spin and mass evolution equations (Equations 64, 62) take the form

$$\frac{dj}{d\tau} = \frac{\dot{\mu}_g}{\mu_\bullet} \left(l_I(j) - 2\epsilon_I(j)j \right), \quad (\text{E13})$$

$$\frac{d\mu_\bullet}{d\tau} = \epsilon_I(j)\dot{\mu}_g. \quad (\text{E14})$$

where $e_I = \left(1 - \frac{2}{3x_I} \right)^{\frac{1}{2}}$, $l_I = \frac{2}{3\sqrt{3}} r_g (1 + 2(3x_+ - 2)^{\frac{1}{2}})$ (Bardeen 1970). The solution of j as a function of black hole mass when there is only accretion present was derived by Bardeen (1970) using the solution of the geodesic equation for the Kerr metric found by Felice (1968) and Carter (1968) to be

$$j = \frac{1}{3} x_+^{\frac{1}{2}} (4 - (3x_+ - 2)^{\frac{1}{2}}), \quad (\text{E15})$$

where $x_I = r_I/r_g$, $x_+ = r_+/r_g$, where r_+ is the horizon, e_I is the energy per unit mass, and l_I is the angular momentum per unit mass for the ISCO. The value of x varies from 6 to 1 for j varying from 0 to 1. Equation (E15), is derived as follows. Using the expressions of l_I and e_I (Bardeen et al. 1972),

$$l_I = \frac{\sqrt{x_I}(x_I^2 + j^2 - 2j\sqrt{x_I})}{x_I(x_I^2 - 3x_I + 2j\sqrt{x_I})^{1/2}}, \quad e_I = \frac{(x_I^2 - 2x_I + j\sqrt{x_I})}{x_I(x_I^2 - 3x_I + 2j\sqrt{x_I})}, \quad (\text{E16})$$

and after squaring both sides we finally arrive at a quadratic equation of j given as

$$3j^2 + 6x_I - 8j\sqrt{x_I} - x_I^2 = 0, \quad (\text{E17})$$

whose solution is

$$j = \frac{\sqrt{x_I}}{3}(4 \pm \sqrt{3x_I - 2}). \quad (\text{E18})$$

Since $j < 1$, the negative sign is the correct choice, so that

$$j(x_+) = \frac{1}{3}x_+^{\frac{1}{2}}(4 - (3x_+ - 2)^{\frac{1}{2}}). \quad (\text{E19})$$

Now, the condition $V_{eff} = \frac{e_I^2 - 1}{2}$ along with Equation (6) in RM19 with $Q = 0$, after some algebra, gives

$$l_I = je_I \pm \frac{x_I}{\sqrt{3}}. \quad (\text{E20})$$

The final expression for l_I becomes (Bardeen et al. 1972),

$$l_I = \frac{2}{3\sqrt{3}}[2(3x_I - 2)^{1/2} + 1] + \frac{x_I}{\sqrt{3}}(-1 \pm 1). \quad (\text{E21})$$

Here a positive sign is the correct choice since for $a = 1$, $l_I = 0$. Therefore, the final expression of l_I is

$$l_I(x_I, m_d) = \frac{2}{3\sqrt{3}}m_d(1 + 2(3x_I - 2)^{\frac{1}{2}}), \quad (\text{E22})$$

where m_d is the mass of the disk consumed by the hole. The analytic relation between x_+ and r_g (Bardeen 1970) is

$$\left(\frac{x_+}{x_1}\right) = \left(\frac{r_{g1}}{r_g}\right)^2, \quad (\text{E23})$$

where x_1 and r_{g1} are the initial values when $j = 0$. Using this, it is found that (Bardeen 1970),

$$\frac{r_g}{r_{g1}} = \left(\frac{3x_1}{2} - 1\right)^{\frac{1}{2}} \sin \left[\left(\frac{2}{3x_1}\right)^{\frac{1}{2}} \frac{\Delta m_0}{r_{g1}} \right] + \cos \left[\left(\frac{2}{3x_1}\right)^{\frac{1}{2}} \frac{\Delta m_0}{r_{g1}} \right], \quad (\text{E24})$$

where Δm_0 is the accreted rest mass when the change in mass is from r_g to r_{g1} . We obtained $j(\mu_\bullet)$ for the Bardeen (1970) solution using Equations (E13) and (E14) where there is only accretion, which is shown in Figure 22. After the black hole spin saturates, only the mass increases, leaving the spin parameter unchanged at the saturated value of 1.

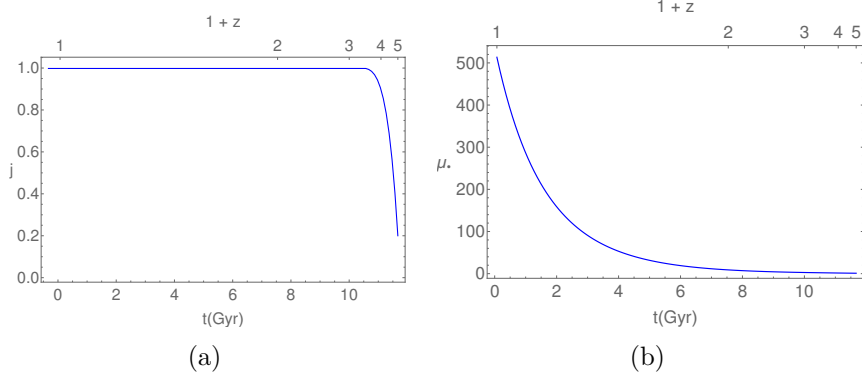


Figure 22. (a) Spin evolution, $j(t)$, and (b) the mass evolution, $\mu_{\bullet}(t)$, for $B_4 = 5$, $z_f = 4$, $\eta = 0.09$, $M_s = 10^5 M_{\odot}$ are shown for the case when only accretion is present (run # 1.2).

Figure 22 shows the solutions to Equations (E13) and (E14), $j(t)$ and $\mu_{\bullet}(t)$, when there is only gas accretion present. The mass continues to grow and the spin reaches a saturated value, and afterward it remains the same.

F. EXPERIMENT 2: NON - RELATIVISTIC ACCRETION FEEDBACK AND FULL LOSS CONE THEORY

Full loss cone theory: Here we consider the case of the full loss cone ($\theta_d \gg \theta_{\ell}$) where the mass density in the galaxy cusp follows a single power-law profile and the stars are able to quickly fill the loss cone on dynamical time scales. Therefore,

$$\rho = \rho_0 r^{-\gamma}, \quad (\text{F25})$$

where γ is the power-law index. The distribution function of stars in a such a galaxy is given by (Merritt 2013a)

$$f_s(E) = \frac{3 - \gamma}{8} \sqrt{\frac{2}{\pi^5}} \frac{\Gamma(\gamma + 1)}{\Gamma(\gamma - \frac{1}{2})} \frac{M_{\bullet}}{m_{\star}} \frac{\phi_0^{\frac{3}{2}}}{(GM_{\bullet})^3} \left(\frac{|E|}{\phi_0} \right)^{\gamma - \frac{3}{2}}, \quad (\text{F26})$$

where $\phi_0 = \frac{GM_{\bullet}}{r_m}$, E is the energy, r_m is the gravitational influence radius of the black hole defined as GM_{\bullet}/σ^2 and m_{\star} is the stellar mass. The rate of capture of stars within the loss cone is

$$F_f(E) = 4\pi^2 L_{\ell}^2(E) f_s(E), \quad (\text{F27})$$

where $L_{\ell}(E)$ is the loss cone angular momentum of the star. An integration of this over all energies gives the total rate of capture in the loss cone,

$$\dot{N}_f = \int_{-\infty}^{\phi_0} F_f(E) dE, \quad (\text{F28})$$

so that

$$\dot{M}_{\bullet \star f} = m_{\star} \dot{N}_f = \frac{3 - \gamma}{8} \sqrt{\frac{1}{2\pi}} \frac{\Gamma(\gamma + 1)}{\Gamma(\gamma - \frac{1}{2})} \frac{l_{\ell}^2}{GM_{\bullet} r_m} \frac{1}{r_m^3} \left(\frac{GM_{\bullet}}{r_m^3} \right)^{\frac{1}{2}} M_{\bullet} = \frac{3 - \gamma}{8} \sqrt{\frac{1}{2\pi}} \frac{\Gamma(\gamma + 1)}{\Gamma(\gamma - \frac{1}{2})} \frac{l_{\ell}^2(M_{\bullet})}{Gc^2} \sigma^5, \quad (\text{F29})$$

where $L_\ell \equiv (GM_\bullet/c) l_\ell$. For the nonrelativistic case, L_ℓ is given by Equation (25). After simplification, it is seen that this expression for $\dot{M}_{\bullet*} \propto \sigma^5$ for the nonrelativistic case does not depend on M_\bullet . However, for the relativistic case, $\dot{M}_{\bullet*}$ depends on both σ and M_\bullet through the capture radius. In the full loss cone regime, the depleted orbits are repopulated within orbital periods by the relaxation process; this is a reasonable assumption for $M_\bullet \ll 10^5 M_\odot$.

Now, we study the nonrelativistic case with no spin and full loss cone theory applied to stellar capture for which a fully analytic solution can be obtained. We solve the mass evolution equation (Equation (58)) to find that

$$t(M_\bullet) = \begin{cases} \int_{M_s}^{M_\bullet} \frac{dM_\bullet}{M_g + M_*} & \text{for } t > t_s \\ t_s + \int_{M_{\bullet t}}^{M_\bullet} \frac{dM_\bullet}{M_*} & \text{for } t \leq t_s, \end{cases} \quad (\text{F30})$$

where t_s is time at which feedback has stopped accretion. Solving Equation (F30) using Equation (11) for \dot{M}_g and Equation (F29) for \dot{M}_* for $t \leq t_s$, we find $\tau_s = k_1 t_s$ where

$$\tau_s = \log \left[\frac{k_1 M_{\bullet t} + k_2 \sigma^5}{k_1 M_s + k_2 \sigma^5} \right] = k_1 t_z(z_s) - k_1 t_z(z_f), \quad (\text{F31})$$

where $M_* = k_2 \sigma^5$ for the nonrelativistic full loss cone theory and k_1 is defined by Equation (9). Using Equation (69), it is found that

$$\left(\tau_s + k_1 t_z(z_f) - k_1 \frac{2}{3} \frac{1}{\sqrt{1 - \Omega_m}} \log \sqrt{1 - \Omega_m} \right) \frac{3\sqrt{1 - \Omega_m}}{2k_1} = \log(\alpha_1 + \sqrt{\Omega_m + \alpha_1^2}), \quad (\text{F32})$$

where

$$\alpha_1^2 = \frac{1 - \Omega_m}{(1 + z_s)^3}.$$

Writing the left-hand side of Equation (F32) as $\log \beta_1$, we derive

$$z_s = \left[\frac{2\beta_1 \sqrt{1 - \Omega_m}}{\beta_1^2 - \Omega_m} \right]^{\frac{2}{3}} - 1. \quad (\text{F33})$$

After solving Equation (F30) for $t > t_s$, the final equation for M_\bullet as a function of redshift is given by

$$M_\bullet(\tau, M_s, \sigma_{100}) = \begin{cases} \mu_M(\tau) M_s + M_s = M_s + (e^\tau + C \sigma_{100}^5 (e^\tau - 1)) M_s & \text{for } z < z_s \\ M_{\bullet t} + [\mu_s + (\tau - \tau_s) C \sigma_{100}^5] M_s & \text{for } z \geq z_s, \end{cases} \quad (\text{F34})$$

where $C = k_2 (100 \text{ km sec}^{-1})^5 / (k_1 M_s)$ and

$$\mu_M = \frac{M_\bullet - M_s}{M_s} = \mu_\bullet - 1, \quad (\text{F35})$$

where $M_s = f_b M_b \sigma^5$.

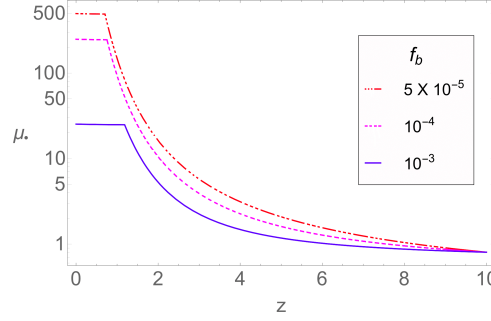


Figure 23. Mass evolution, $\mu_{\bullet}(z)$, is shown for different f_b for $\sigma_{100} = 1$ (run #2.1, #2.2, #2.3) with $j_0 = 0$, $B_4 = 0$.

In Figure 23, the late evolution represents the black hole mass growth only by capture of stars, and the mass growth rate by accretion of gas dominates much earlier.

1. In the later experiments, we have scaled Equation (64) by Equation (62) to obtain an equation for $\frac{dj}{dM_{\bullet}}$ that is solved to find $j(M_{\bullet})$ and fed into Equation (62) to obtain $M_{\bullet}(t)$.
2. We derive $j(t)$ similarly, using the solution of $j(M_{\bullet})$ in Equation (64).
3. All the solutions are dependent on the value of σ which we have considered to be constant throughout for a particular galaxy.

G. EXPERIMENT 3: EFFECT OF GAS ACCRETION AND BZ TORQUE

Here the spin and mass evolution equations (Equations 64, 62) take the form

$$\frac{dj}{d\tau} = \frac{\dot{\mu}_g}{\mu_{\bullet}} \left(l_I(j) - 2\epsilon_I(j)j \right) + \frac{4}{9} \times 10^{-5} f_{BZ} B_4 \mu_{\bullet} M_{s5} x_+^3(j) j. \quad (\text{G36})$$

$$\frac{d\mu_{\bullet}}{d\tau} = \epsilon_I(j) \dot{\mu}_g. \quad (\text{G37})$$

First, we study the canonical case (run # 3.1.1, experiment 3), and then we change the parameters one by one, keeping others constant. We now present the results for different runs listed in Table 5.

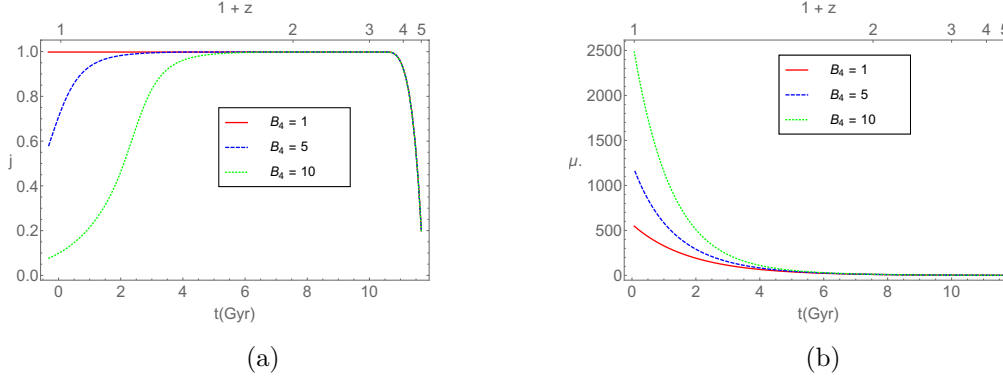


Figure 24. (a) Spin evolution, $j(t)$, and (b) mass evolution, $\mu_{\bullet}(t)$, are shown for run# 3.1.1 and run # 3.1.2 in Table 5 when there is only accretion and BZ torque present.

1. It can be seen from Figure 24(a) that the BZ torque causes the spin-down of the black hole reducing it from the highest saturated spin value. As the B_4 value is increased, the spin-down is more effective while the accretion is enhanced.

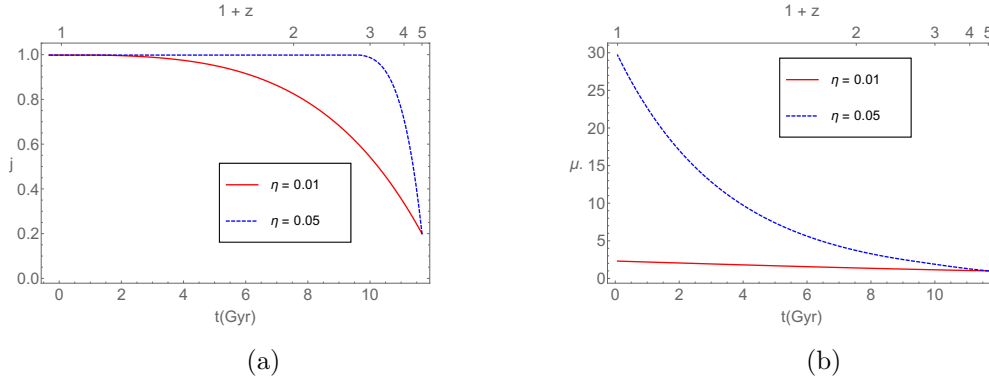


Figure 25. (a) Spin evolution, $j(t)$, and (b) mass evolution, $\mu_{\bullet}(t)$, are shown for run # 3.2.1 and # 3.2.2 [see Table 5] when there is only accretion and BZ torque present.

2. From the plots (see Figure 25) it can be seen that mass growth by accretion with an efficiency of $\eta = 0.01$ or 0.05 is very small, which cannot generate high-mass black holes in the universe, indicating that $\eta \geq 0.05$.

H. EXPERIMENT 4: GAS ACCRETION, STELLAR CAPTURE, AND BZ TORQUE ARE PRESENT

In this experiment, the spin and mass evolution equations (Equations 64, 62) take the form

$$\frac{dj}{d\tau} = \frac{\dot{\mu}_g}{\mu_{\bullet}} \left(l_I(j) - 2\epsilon_I(j)j \right) + \frac{\dot{\mu}_{\star}}{\mu_{\bullet}} \left(l_{\star}(j) - 2\epsilon(j)j \right) + \frac{4}{9} \times 10^{-5} f_{BZ} B_4 \mu_{\bullet} M_{s5} x_+^3(j) j. \quad (\text{H38})$$

$$\frac{d\mu_{\bullet}}{d\tau} = \epsilon_I(j) \dot{\mu}_g + \epsilon(j) \dot{\mu}_{\star}. \quad (\text{H39})$$

where accretion, BZ torque, and the stellar capture with steady loss cone theory are taken into account.

1. By studying the canonical case (run # 2.1), we find that the mass evolution does not show any significant variation with changes in parameters (k, γ, j_0) and the spin evolution does not show variation for changes in (k, γ) . This is because the accretion is a dominant process and the factors that control the stellar capture do not make a significant impact on the range of parameters considered.

We present the results and discuss the runs (# 4.1 to # 4.6) given in Table 5.

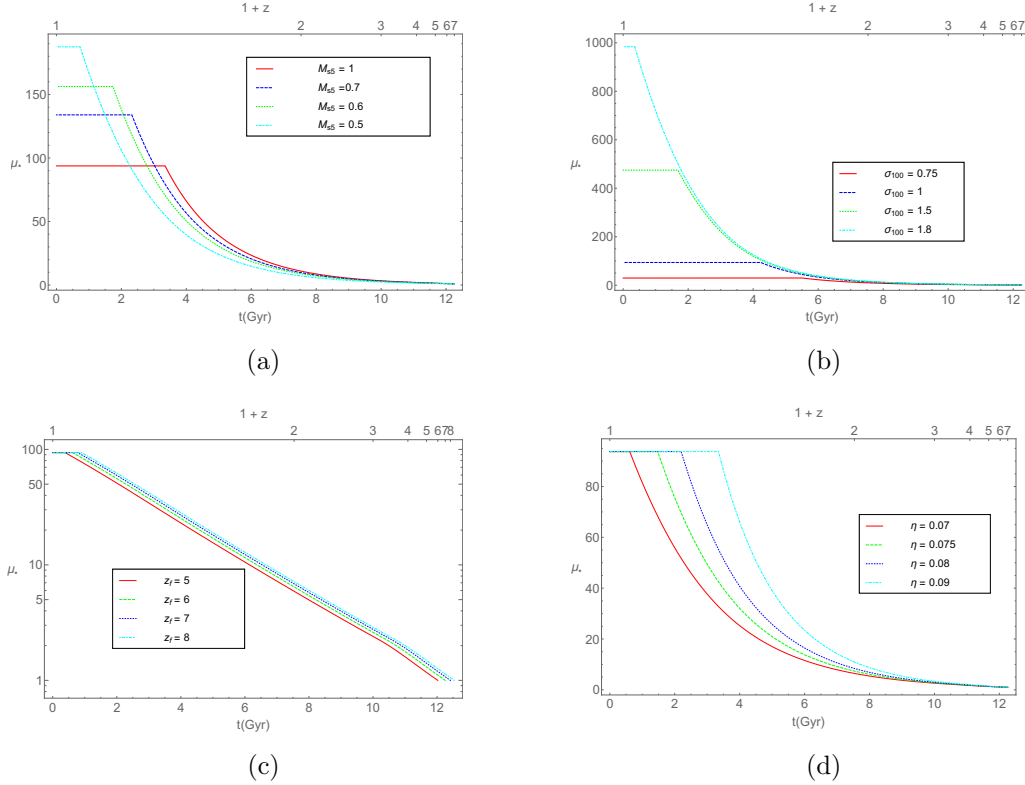


Figure 26. Mass evolution, $\mu_{\bullet}(t)$, for run # 4.1, # 4.3, # 4.4, # 4.5 [see Table 5] (a – d) are shown, for the case when there is accretion, stellar capture and BZ torque present.

1. Figure 26 show the evolution of black hole mass for run # 4.1 to run # 4.5 given in Table 5. We see by studying its deviation from the canonical set that the evolution has a small dependence on the parameters $\{k, \gamma, j_0, B_4\}$, so we do not show those cases here.
2. If the σ is the same, then the final mass will be almost the same, irrespective of their initial masses [see Figure 26(a)].
3. Change in z_f (run # 4.4) makes little impact on the evolution and does not affect the final mass much [see Figure 26(c)].
4. Variation of σ (run # 4.3) shifts the saturation point owing to the dependence on σ [see Equation (57)]. The higher the σ , the higher the saturation mass, and longer the time taken to reach the saturation point [see Figure 26(b)].

5. Increase of η (run # 4.5) increases the accretion rate, which is the main source of mass growth. Hence, for higher η , the system reaches the saturation point earlier [see Figure 26(d)].

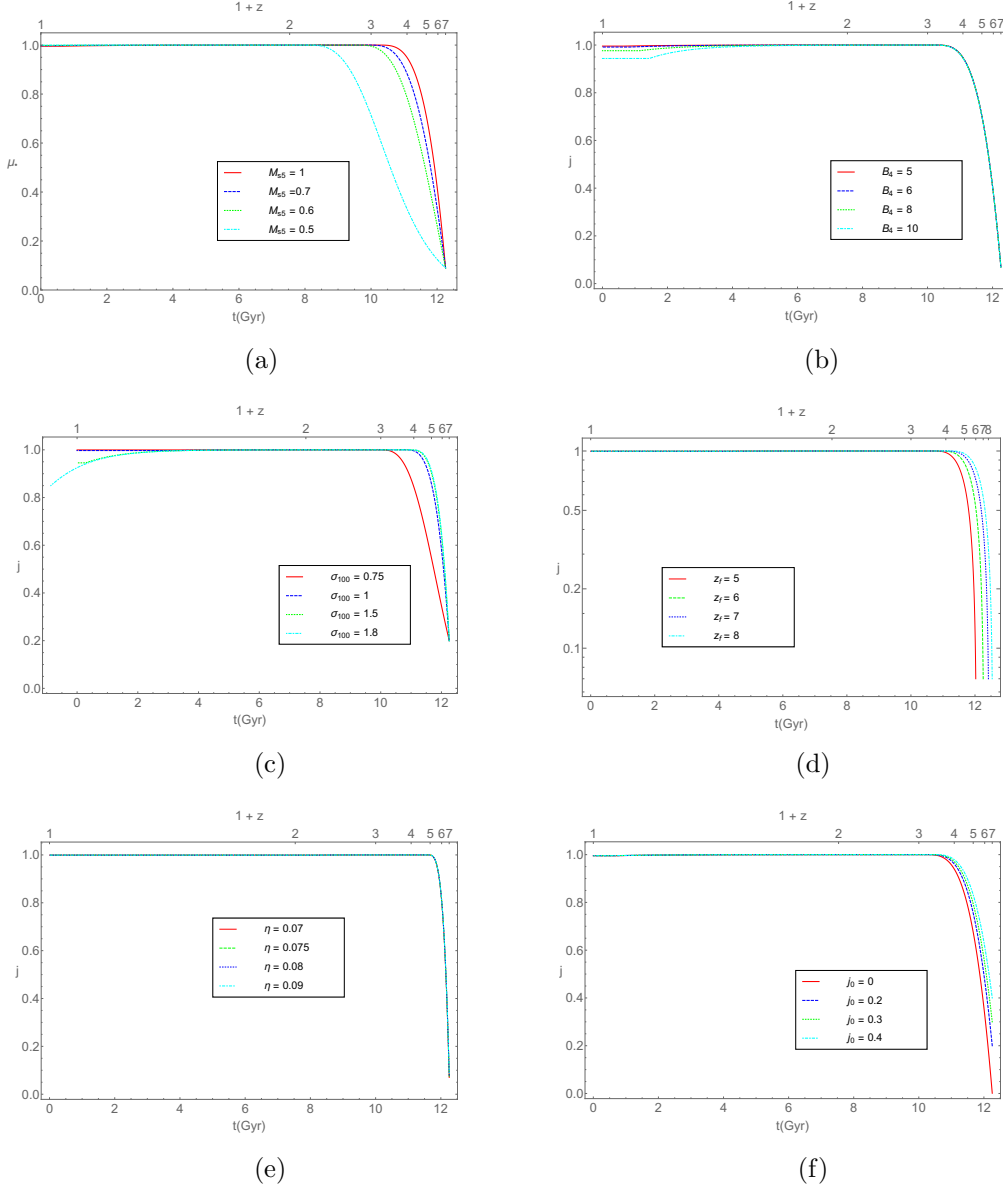


Figure 27. Spin evolution, $j(t)$, for run # 4.1 to run # 4.6 (a – f) [see Table 5] are shown, for the cases when there is accretion, stellar capture, and BZ torque present.

6. The spin j has a smaller dependence on the initial parameters $\{M_s, z_f, \eta, j_0\}$ [run # 4.1, # 4.4, # 4.5, # 4.6, respectively; see Figures 27(a), 27(d), 27(e), 27(f)], where a variation is seen at the starting points because of different initial values, but the final values attained are nearly the same. This result is different from that of experiment 3, where only accretion is present; we incorporate the concept of saturated mass here, which causes the accretion to stop, thereby reducing the final mass attained.

7. The decrease in j occurs at the high-mass end because of the BZ effect, which is small compared to the run # 3.1.1 [see Figure 27(b)]. This is because, in experiment 3, we did not incorporate the saturation of black hole mass, which resulted in a high final mass reducing j owing to the BZ effect. It is also seen that an increase in B_4 value (run # 4.2) decreases the final spin, as expected.
8. A higher σ (run # 4.3) causes a higher final mass of the black hole; hence, the final spin value decreases with an increase in σ , (see Figure 27(c)) while keeping M_s constant.

REFERENCES

- Alexander, T., & Bar-Or, B. 2017, *Nature Astronomy*, 1, 0147
- Bardeen, J. M. 1970, *Nature*, 226, 64
- Bardeen, J. M. 1973, in *Black Holes (Les Astres Occlus)*, ed. C. Dewitt & B. S. Dewitt, 215–239
- Bardeen, J. M., Press, W. H., & Teukolsky, S. A. 1972, *ApJ*, 178, 347
- Batiste, M., Bentz, M. C., Raimundo, S. I., Vestergaard, M., & Onken, C. A. 2017, *ApJL*, 838, L10
- Bezanson, R., van Dokkum, P. G., Tal, T., et al. 2009, *ApJ*, 697, 1290
- Bhattacharyya, D., & Mangalam, A. 2018, *Journal of Astrophysics and Astronomy*, 39, 4
- Bhattacharyya, D., & Mangalam, A. 2018, *Proceedings of the International Astronomical Union*, 14, 254256
- Blandford, R. D., Netzer, H., Woltjer, L., Courvoisier, T. J.-L., & Mayor, M., eds. 1990, *Active Galactic Nuclei*, 97
- Blandford, R. D., & Znajek, R. L. 1977, *MNRAS*, 179, 433
- Boco, L., Lapi, A., & Danese, L. 2020, *ApJ*, 891, 94
- Brenneman, L. W., & Reynolds, C. S. 2006, *ApJ*, 652, 1028
- Brockamp, M., Baumgardt, H., & Kroupa, P. 2011, *MNRAS*, 418, 1308
- Campitiello, S., Celotti, A., Ghisellini, G., & Sbarrato, T. 2019, *A&A*, 625, A23
- Carter, B. 1968, *Phys. Rev.*, 174, 1559. <https://link.aps.org/doi/10.1103/PhysRev.174.1559>
- Carter, B. 1968, *Physical Review*, 174, 1559
- Cohn, H., & Kulsrud, R. M. 1978, *ApJ*, 226, 1087
- Davis, S. W., & Laor, A. 2011, *ApJ*, 728, 98
- Debbatista, V. P., Kazantzidis, S., & van den Bosch, F. C. 2013, *ApJ*, 765, 23
- Donley, J. L., Brandt, W. N., Eracleous, M., & Boller, T. 2002, *AJ*, 124, 1308
- Dubois, Y., Volonteri, M., & Silk, J. 2014, *MNRAS*, 440, 1590
- Felice, F. 1968, *Nuovo Cimento B Serie*, 57, 351
- Ferrarese, L. 2002, *ApJ*, 578, 90
- Ferrarese, L., & Ford, H. 2005, *SSRv*, 116, 523
- Ferrarese, L., & Merritt, D. 2000, *ApJL*, 539, L9
- Frank, J., & Rees, M. J. 1976, *MNRAS*, 176, 633
- Frolov, V. P., & Novikov, I. D. 1998, *Black hole physics : basic concepts and new developments*
- Gammie, C. F., Shapiro, S. L., & McKinney, J. C. 2004, *ApJ*, 602, 312
- Gebhardt, K., Bender, R., Bower, G., et al. 2000, *ApJL*, 539, L13
- Gezari, S., Heckman, T., Cenko, S. B., et al. 2009, *ApJ*, 698, 1367
- Gültekin, K., Richstone, D. O., Gebhardt, K., et al. 2009, *ApJ*, 698, 198
- Hopkins, P. F., Bundy, K., Murray, N., et al. 2009, *MNRAS*, 398, 898
- Hughes, S. A., & Blandford, R. D. 2003, *ApJL*, 585, L101
- Jahnke, K., & Macciò, A. V. 2011, *ApJ*, 734, 92
- Kesden, M. 2012, *PhRvD*, 85, 024037
- Kesden, M., Lockhart, G., & Phinney, E. S. 2010, *PhRvD*, 82, 124045
- King, A. 2003, *ApJL*, 596, L27
- King, A. R., Pringle, J. E., & Hofmann, J. A. 2008, *MNRAS*, 385, 1621
- Komossa, S. 2015, *Journal of High Energy Astrophysics*, 7, 148
- Kormendy, J., & Ho, L. C. 2013, *ARA&A*, 51, 511
- Kormendy, J., & Richstone, D. 1995, *ARA&A*, 33, 581
- Kravtsov, A. V., Berlind, A. A., Wechsler, R. H., et al. 2004, *ApJ*, 609, 35

- Kravtsov, A. V., Klypin, A. A., & Khokhlov, A. M. 1997, *ApJS*, 111, 73
- Lapi, A., Raimundo, S., Aversa, R., et al. 2014, *ApJ*, 782, 69
- Li, L.-X. 2012, *MNRAS*, 424, 1461
- Mageshwaran, T., & Mangalam, A. 2015, *ApJ*, 814, 141
- Magorrian, J., & Tremaine, S. 1999, *MNRAS*, 309, 447
- Mangalam, A. 2001, *A&A*, 379, 1138
- Mangalam, A. 2015, in *Astronomical Society of India Conference Series*, Vol. 12, *Astronomical Society of India Conference Series*, 51–56
- Mangalam, A., Gopal-Krishna, & Wiita, P. J. 2009, *MNRAS*, 397, 2216
- Marronetti, P., Tichy, W., Brüggmann, B., González, J., & Spherhake, U. 2008, *PhRvD*, 77, 064010
- McConnell, N. J., & Ma, C.-P. 2013, *ApJ*, 764, 184
- Merritt, D. 2013a, *Classical and Quantum Gravity*, 30, 244005
- . 2013b, *Dynamics and Evolution of Galactic Nuclei*
- Merritt, D., & Ferrarese, L. 2001, *ApJ*, 547, 140
- Misner, C. W., Thorne, K. S., & Wheeler, J. A. 1973, *Gravitation*
- Mo, H., van den Bosch, F. C., & White, S. 2010, *Galaxy Formation and Evolution*
- Netzer, H. 2010, in *IAU Symposium*, Vol. 267, *Co-Evolution of Central Black Holes and Galaxies*, ed. B. M. Peterson, R. S. Somerville, & T. Storchi-Bergmann, 213–222
- Oser, L., Naab, T., Ostriker, J. P., & Johansson, P. H. 2012, *ApJ*, 744, 63
- Pandey, K. L., & Mangalam, A. 2018, *Journal of Astrophysics and Astronomy*, 39, 9
- Rana, P., & Mangalam, A. 2019a, *Classical and Quantum Gravity*, 36, 045009
- . 2019b, *arXiv e-prints*, arXiv:1901.02730
- Rauch, K. P., & Ingalls, B. 1998, *MNRAS*, 299, 1231
- Rauch, K. P., & Tremaine, S. 1996, *NewA*, 1, 149
- Robertson, B., Hernquist, L., Cox, T. J., et al. 2006, *ApJ*, 641, 90
- Sahu, N., Graham, A. W., & Davis, B. L. 2019, *ApJ*, 887, 10
- Salucci, P., Szuszkiewicz, E., Monaco, P., & Danese, L. 1999, *MNRAS*, 307, 637
- Salviander, S., & Shields, G. A. 2013, *ApJ*, 764, 80
- Schulze, A., & Wisotzki, L. 2010, *A&A*, 516, A87
- Shankar, F. 2013, *Classical and Quantum Gravity*, 30, 244001
- Shankar, F., Bernardi, M., & Haiman, Z. 2009a, *ApJ*, 694, 867
- Shankar, F., Weinberg, D. H., & Miralda-Escudé, J. 2009b, *ApJ*, 690, 20
- Shankar, F., Weinberg, D. H., Marsden, C., et al. 2020, *MNRAS*, 493, 1500
- Shapiro, S. L. 2005, *ApJ*, 620, 59
- Shen, Y., Greene, J. E., Strauss, M. A., Richards, G. T., & Schneider, D. P. 2008, *ApJ*, 680, 169
- Shen, Y., Greene, J. E., Ho, L. C., et al. 2015, *ApJ*, 805, 96
- Sijacki, D., Vogelsberger, M., Genel, S., et al. 2015, *MNRAS*, 452, 575
- Silk, J., & Rees, M. J. 1998, *A&A*, 331, L1
- Stewart, K. R., Bullock, J. S., Barton, E. J., & Wechsler, R. H. 2009, *ApJ*, 702, 1005
- Suh, H., Hasinger, G., Steinhardt, C., Silverman, J. D., & Schramm, M. 2015, *ApJ*, 815, 129
- Syer, D., & Ulmer, A. 1999, *MNRAS*, 306, 35
- Taylor, P., & Kobayashi, C. 2016, *MNRAS*, 463, 2465
- Thorne, K. S. 1974, *ApJ*, 191, 507
- Thorp, S., Chadwick, E., & Sesana, A. 2019, *MNRAS*, 488, 4042
- Tremaine, S., Gebhardt, K., Bender, R., et al. 2002, *ApJ*, 574, 740
- Volonteri, M., Madau, P., Quataert, E., & Rees, M. J. 2005, *ApJ*, 620, 69
- Volonteri, M., & Rees, M. J. 2005, *ApJ*, 633, 624
- Wang, J., & Merritt, D. 2004, *ApJ*, 600, 149
- Wetzel, A. R., Cohn, J. D., & White, M. 2009, *MNRAS*, 395, 1376
- Xiao, T., Barth, A. J., Greene, J. E., et al. 2011, *ApJ*, 739, 28
- Zhang, X., & Lu, Y. 2019, *ApJ*, 873, 101
- Zhao, H., Haehnelt, M. G., & Rees, M. J. 2002, *NewA*, 7, 385